



This is a repository copy of *Design, development, and evaluation of a contactless respiration rate measurement device utilizing a self-heating thermistor.*

White Rose Research Online URL for this paper:

<https://eprints.whiterose.ac.uk/228041/>

Version: Published Version

---

**Article:**

Saatchi, R. [orcid.org/0000-0002-2266-0187](https://orcid.org/0000-0002-2266-0187), Holloway, A., Travis, J. et al. (7 more authors) (2025) Design, development, and evaluation of a contactless respiration rate measurement device utilizing a self-heating thermistor. *Technologies*, 13 (6). 237. ISSN 2227-7080

<https://doi.org/10.3390/technologies13060237>

---

**Reuse**

This article is distributed under the terms of the Creative Commons Attribution (CC BY) licence. This licence allows you to distribute, remix, tweak, and build upon the work, even commercially, as long as you credit the authors for the original work. More information and the full terms of the licence here:

<https://creativecommons.org/licenses/>

**Takedown**



If you consider content in White Rose Research Online to be in breach of UK law, please notify us by emailing [eprints@whiterose.ac.uk](mailto:eprints@whiterose.ac.uk) including the URL of the record and the reason for the withdrawal request.



[eprints@whiterose.ac.uk](mailto:eprints@whiterose.ac.uk)  
<https://eprints.whiterose.ac.uk/>

## Article

# Design, Development, and Evaluation of a Contactless Respiration Rate Measurement Device Utilizing a Self-Heating Thermistor

Reza Saatchi <sup>1,\*</sup> , Alan Holloway <sup>1</sup>, Johnathan Travis <sup>1</sup>, Heather Elphick <sup>2</sup>, William Daw <sup>2</sup>, Ruth N. Kingshott <sup>2</sup>, Ben Hughes <sup>3</sup>, Derek Burke <sup>1</sup>, Anthony Jones <sup>4</sup>  and Robert L. Evans <sup>5</sup>

<sup>1</sup> School of Engineering & Built Environment, Sheffield Hallam University, City Campus, Howard Street, Sheffield S1 1WB, UK; a.f.holloway@shu.ac.uk (A.H.); j.r.travis@shu.ac.uk (J.T.); derek.paburke@gmail.com (D.B.)

<sup>2</sup> Sheffield Children's NHS Foundation Trust, Clarkson Street, Broomhall, Sheffield S10 2TH, UK; h.elphick@nhs.net (H.E.); william.daw1@nhs.net (W.D.); ruth.kingshott@nhs.net (R.N.K.)

<sup>3</sup> School of Mechanical, Aerospace and Civil Engineering, The University of Sheffield, Western Bank, Sheffield S10 2TN, UK; ben.hughes@sheffield.ac.uk

<sup>4</sup> Art, Design and Media Research Centre, Sheffield Hallam University, City Campus, Howard Street, Sheffield S1 1WB, UK; a.jones@shu.ac.uk

<sup>5</sup> Research & Innovation Office, Cranfield University, Cranfield Campus, College Road, Cranfield MK43 0AL, UK; rob.l.evans@cranfield.ac.uk

\* Correspondence: r.saatchi@shu.ac.uk

**Abstract:** The respiration rate (RR) is an important vital sign for early detection of health deterioration in critically unwell patients. Its current measurement has limitations, relying on visual counting of chest movements. The design of a new RR measurement device utilizing a self-heating thermistor is described. The thermistor is integrated into a hand-held air chamber with a funnel attachment to sensitively detect respiratory airflow. The exhaled respiratory airflow reduces the temperature of the thermistor that is kept at a preset temperature, and its temperature recovers during inhalation. A microcontroller provides signal processing, while its display screen shows the respiratory signal and RR. The device was evaluated on 27 healthy adult volunteers, with a mean age of 32.8 years (standard deviation of 8.6 years). The RR measurements from the device were compared with the visual counting of chest movements, and the contact method of inductance plethysmography that was implemented using a commercial device (SOMNOtouch™ RESP). Statistical analysis, e.g., correlations were performed. The RR measurements from the new device and SOMNOtouch™ RESP, averaged across the 27 participants, were 14.6 breaths per minute (bpm) and 14.0 bpm, respectively. The device has a robust operation, is easy to use, and provides an objective measure of the RR in a noncontact manner.

**Keywords:** noncontact respiration rate measurement; digital healthcare device; medical electronics; medical devices; medical engineering



Academic Editors: Luc de Witte and Dennis Douroumis

Received: 10 April 2025

Revised: 20 May 2025

Accepted: 6 June 2025

Published: 9 June 2025

**Citation:** Saatchi, R.; Holloway, A.; Travis, J.; Elphick, H.; Daw, W.; Kingshott, R.N.; Hughes, B.; Burke, D.; Jones, A.; Evans, R.L. Design, Development, and Evaluation of a Contactless Respiration Rate Measurement Device Utilizing a Self-Heating Thermistor. *Technologies* **2025**, *13*, 237. <https://doi.org/10.3390/technologies13060237>

**Copyright:** © 2025 by the authors. Licensee MDPI, Basel, Switzerland. This article is an open access article distributed under the terms and conditions of the Creative Commons Attribution (CC BY) license (<https://creativecommons.org/licenses/by/4.0/>).

## 1. Introduction

Breathing and respiration involve a sequence of events that include air entering the lungs and oxygen from the inhaled air diffusing from the alveoli into pulmonary capillaries surrounding them and binding to the haemoglobin molecules in red blood cells. The oxygen is transferred to the tissues by the red blood cells, where it is converted to energy, and the resulting carbon dioxide is exhaled [1]. The respiration rate (RR) is the average number of breaths (inhalation and exhalation cycles) per minute, which is defined in units

of breaths per minute (bpm). The RR in healthy adults is typically 12–20 bpm [2]. A study reported the median RR in children from birth to the age of 18 years [3]. According to the study, the median RR in children reduces from around 44 bpm from birth to around 37 bpm when aged one year. Thereafter, there is a steeper reduction in the RR to about 22 bpm by the age of 6 years and a more gradual reduction to around 15 bpm when aged 18 years.

The RR, body temperature, heart rate, systolic blood pressure, level of consciousness, and blood oxygen saturation level are the main vital signs for monitoring patients. The RR is an early indicator of deterioration in critically ill patients and can be used to predict patients at risk of conditions such as cardiac arrest [4]. Measuring the RR in acute hospital wards at least daily is encouraged [5]. Despite the importance of measuring the RR, it is often missed because of difficulties in its measurement [6–11].

The current method of measuring the RR that involves observing the patient's chest and manually counting its movements for 15 s has limitations [12]. The approach is subjective, and its multiplication by four to obtain the RR in bpm magnifies the measurement error. Manual RR measurement in young children can be more challenging than adults due to their higher RRs and, in some cases, their lack of co-operation.

To overcome the limitations of manual counting of chest movements, several objective RR measurements methods were reported that can broadly be grouped as contact and non-contact. In the contact methods, the sensing element is attached to the subject's body, while in the noncontact methods, the measurement is performed without any body attachment. A comparison of contact and noncontact RR measurement methods in children was carried out, highlighting their strengths and limitations [8]. The study indicated that noncontact RR methods are preferable, especially for children, as they are less disruptive as compared to the contact methods.

The aim of this work was to design, develop, and evaluate a new easy-to-use, accurate, and cost-effective noncontact RR measurement device. The noncontact feature of the device means a less intrusive measurement compared to the contact methods that is particularly valuable in pediatrics. Furthermore, the measurement becomes consistent and objective, as it would not require visual counting of chest movement. The contact RR measurement methods may stress cause stress for paediatric patients and thus inadvertently altering their RR. The new device was primarily designed for children; however, it is also applicable for adults. The device is referred to in this article as the Contactless Pediatric Respiration Monitor (CPRM).

The CPRM uses a self-heating thermistor to detect respiratory airflow and applies signal processing to determine the RR, as discussed in the methodology section. The utilized technique of anemometry is a flow measurement technology with multiple industrial applications. Its advantages include high sensitivity at low flow rates, durability, and robust sensing construction [13]. The use of a self-heating thermistor for anemometry provides high sensitivity to the flow rate, and low power consumption [13]. Some related design considerations were reported in a previous study, in which a thermistor was used as part of a thermal anemometer [14]. The contributions of this study include the following:

- An overview of recent technological developments in RR measurement.
- The design and development of a new, easy-to-use, cost-effective, robust, noncontact RR measurement device.
- A thorough simulation and associated design calculations to establish the operating parameters of the self-heating thermistor for noncontact RR measurement.
- Evaluation of the performance of the new RR measurement device against RR measures obtained by chest movement visual counting and by using a commercial respiratory measurement device called SOMNOtouch™ RESP [15].

In the following sections, an overview of the related literature is provided, the design details are explained, and evaluation results are presented.

## 2. Related Literature Outlining Developments in Respiration Rate Measurement

There are several reviews exploring various developments in measuring the RR, e.g., [8,16–21]. An overview of the RR measurement methods is provided in this section.

The main contact-based RR measurement methods include the following:

- **Pulse-oximetry-based method:** Pulse oximeters use the principle that oxyhemoglobin and deoxyhemoglobin absorb red and near-infrared (IR) light distinctly [22]. The approach measures oxygen saturation in peripheral arterial blood (SpO<sub>2</sub>) [23] and converts it to an electrical signal from which the RR is determined. The method, however, has limitations, e.g., SpO<sub>2</sub> may be normal during an increased RR due to hypercapnia [23].
- **Electrocardiogram (ECG)-derived RR (EDR):** In this approach, the RR is determined from an ECG signal. The method is noninvasive and can be performed in both time and frequency domains. The movement of the chest due to respiration causes the distance between the electrodes used to measure the ECG to vary. This results in dynamic variations in the Q, R, and S features of the ECG [24] from which the RR is determined. A few approaches were reported to determine the RR using the EDR [25]. In the frequency domain, the ECG is band-pass filtered, and its magnitude frequency spectrum is determined by using the discrete Fourier transform (DFT). The frequency associated with the highest peak in the magnitude frequency spectrum is used to determine the RR [24]. The positive aspect of these methods is that an available ECG machine could be utilized for this purpose (new equipment would not be required). However, EDR methods have limitations [26], e.g., signal distortion due to any body movements and its computational complexities.
- **Chest movement tracking:** A variety of approaches were reported for tracking chest movement and converting the information to a respiratory signal. A piezoelectric sensor embedded into a soft elastic band wrapped around the chest produced a signal that, once conditioned and digitized, indicated the RR [27]. Accelerometers placed on the chest converted respiration-related chest movements to an electrical signal [28–32]. In an optical approach, a Mach–Zehnder interferometer (an instrument that measures the relative phase shift variations between two collimated beams produced by splitting light from a single source) has been integrated into a belt worn on the abdomen to provide a means of measuring the RR [33]. In inductive plethysmography, chest movement is typically tracked by two separate bands embedded with conducting wires wrapped around the chest and abdomen. The signals from the bands indicate the RR [34].

These methods may not be very intrusive. However, the contact nature of these methods limits their applicability in environments such as accident and emergency departments, where a quick RR measurement is advantageous.

- **Contact-thermistor-based method:** A thermistor/thermocouple taped under the nose detects an increase in temperature during exhalation and a decrease in temperature during inhalation. The resulting temperature variations produce a respiratory signal generated by the sensor. The approach provides a semiquantitative estimation of respiratory airflow (i.e., an indirect measure). Its operation is nonlinear and has a slow response time [34].
- **Nasal-prongs-based method:** The method provides an indirect measurement of respiratory airflow, relying on the differential pressure of the flow and atmospheric

pressure [35]. The relationship between the measured pressure and the respiratory airflow is nonlinear [35]. The prongs are plastic tubes placed into the nostrils, and a tube connects them to the device measuring the airflow. Some young children do not tolerate the method due to its intrusiveness.

- Thoracic impedance pneumography: Movements of the chest during breathing cause variations in the thoracic impedance, resulting in an RR-related electrical signal [36].

The main noncontact (contactless) RR measurement methods include the following:

- Infrared thermal imaging: The principle associated with this approach is that during exhalation, warmer respiratory air from the lungs increases the skin temperature of the nose, mainly around the nostrils. During inhalation, the environmental air passing through the nose reduces the skin temperature of the region. These temperature fluctuations result in variations in the amount of infrared (IR) radiated from the region. The IR radiation can be measured over time by an IR thermal imaging camera and converted to a respiratory signal. Several studies have developed and evaluated this approach, e.g., [37,38]. The cost of the thermal camera is a consideration in adapting this approach. Furthermore, any large head movement can cause the respiratory region of interest to move out of the field of view of the camera, thus interrupting the measurement.
- Vision-based method: The approach uses a visual camera to track respiration-related chest movement [39–41]. The method is susceptible to background light intensity, body movements, and the effectiveness of the tracking algorithm used to deal with body movement.
- Carbon dioxide sensing: Exhaled respiratory air has a higher concentration of carbon dioxide (CO<sub>2</sub>) in comparison with its concentration in the environment. A noncontact CO<sub>2</sub> sensor detects the variations in the CO<sub>2</sub> concentration in the air near the subject and converts them into a respiratory signal. Recent technological developments have significantly improved the capability of miniature CO<sub>2</sub> sensors [42,43], making this method more practical [20]. The approach is susceptible to distortions such as the presence of another person in the vicinity of the patient being monitored. Sensitive CO<sub>2</sub> sensors are costly and often require a pump to direct the respiratory airflow into the sensor, adding an extra cost.
- Humidity measurement: The moisture level of the exhaled air is typically higher than that of the recording environment. Humidity sensors can detect moisture variations and produce a respiratory-related signal. There are multiple sensor types for this purpose, e.g., nanomaterials coated on a substrate can absorb water molecules changing one or more of their properties [44].
- Respiratory sound measurement: This approach relies on converting the respiratory sounds to an electrical signal using one or more sensitive microphones [45,46]. The method is susceptible to background sounds that could be much stronger in magnitude than the respiratory-related sounds [47].
- Radar-based method: A radar sensor placed in front of the chest detects variations in its distance to the chest during inhalation and exhalation [48–51], thus providing a means of measuring the RR over time. The method can be sensitive, but it is prone to environmental noise [52].
- Ultrasound-based method: The operation of ultrasound (US) is based on acoustic energy with frequencies higher than 20 kHz. A US transceiver (transmitter and receiver) detects the reflected acoustic signal from the chest, converting the variations in its distance to the chest. This approach has been developed and evaluated [53–55].

For ease of comparison of the RR-related studies, a summary table is provided in Table A1 in Appendix A.

### 3. Methodology

In this section, the design of CPRM and its evaluation are described. Initially, an overview of the device's operation is included, and then a more thorough explanation of its parts is provided.

#### 3.1. Overview of CPRM Hardware

The block diagram of CPRM is shown in Figure 1, and its use with a child is shown in Figure 2.

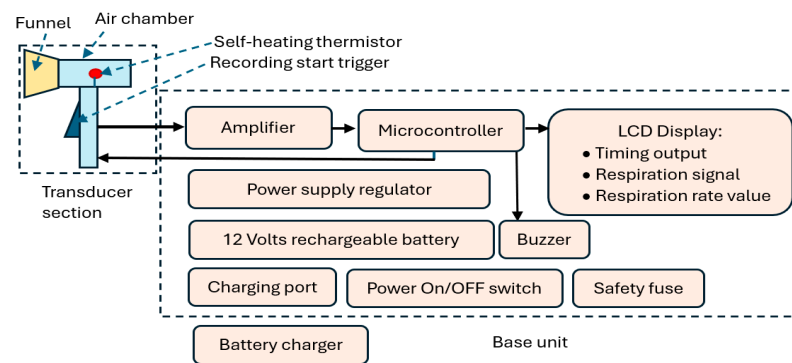


**Figure 1.** CPRM block diagram indicating its main elements.



**Figure 2.** CPRM in use with a child [56].

CPRM consists of two main sections:

- **Section A:** This represents the device's respiratory airflow transducer. It detects the respiratory airflow through its self-heating thermistor located in an air chamber. The air chamber has a funnel attachment for an improved respiratory airflow guidance. The thermistor generates an electrical signal in response to the respiratory airflow. This section also contains the start RR measurement trigger mechanism.
- **Section B:** This is the device's base unit that is connected by a wire to the transducer section (i.e., Section A). It receives the electrical signal from section A and processes it using a microcontroller. The microcontroller communicates with the RR measurement-start trigger mechanism, sends information to an LCD to indicate the recording time (this is count down of time in seconds from the time the trigger is pressed to the final measurement), displays respiratory signal, and shows the value of the RR when measurement is completed. The microcontroller also activates a buzzer indicating RR value is ready to read from the LCD. The base unit contains power supply regulators and a 12 V rechargeable battery. It has ports to connect it to its battery charger. The unit has a power switch ON/OFF button and a safety fuse.

The sections of CPRM are shown in Figure 3a, and the base unit has been opened as depicted in the image to show its electronic circuitry in Figure 3b. Figure 4a shows the



inner parts of the 3D-printed transducer section with the funnel removed, and Figure 4b shows the location of the thermistor. The transducer section was made using a standard 3D printer with the material ABS (Acrylonitrile Butadiene Styrene plastic). The melting range of ABS is about 190–270 °C, and it is generally accepted that it can safely be used without distorting up to 100 °C.

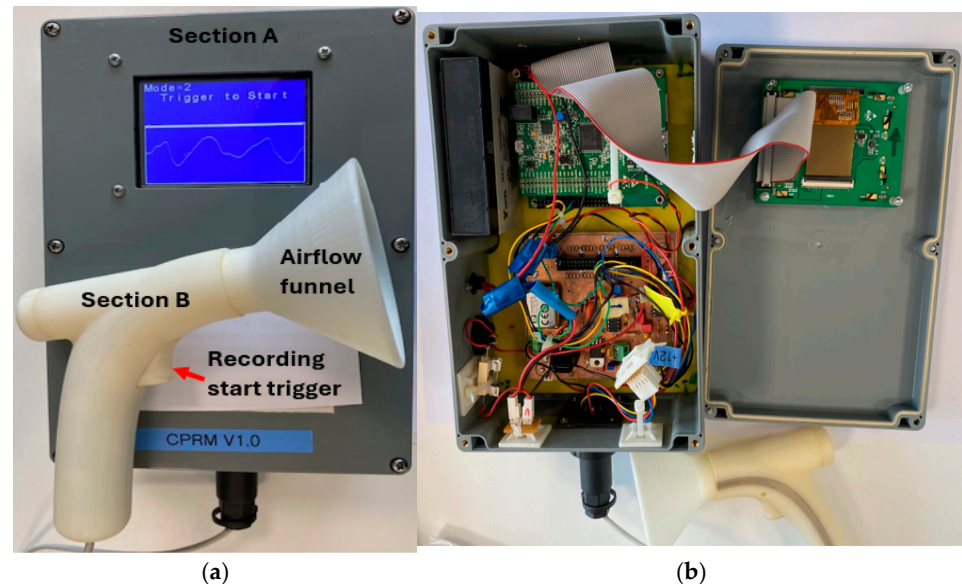


**Figure 3.** (a) A photograph of CPRM displaying its transducer and base units. (b) CPRM base unit case opened to show its electronic circuitry.

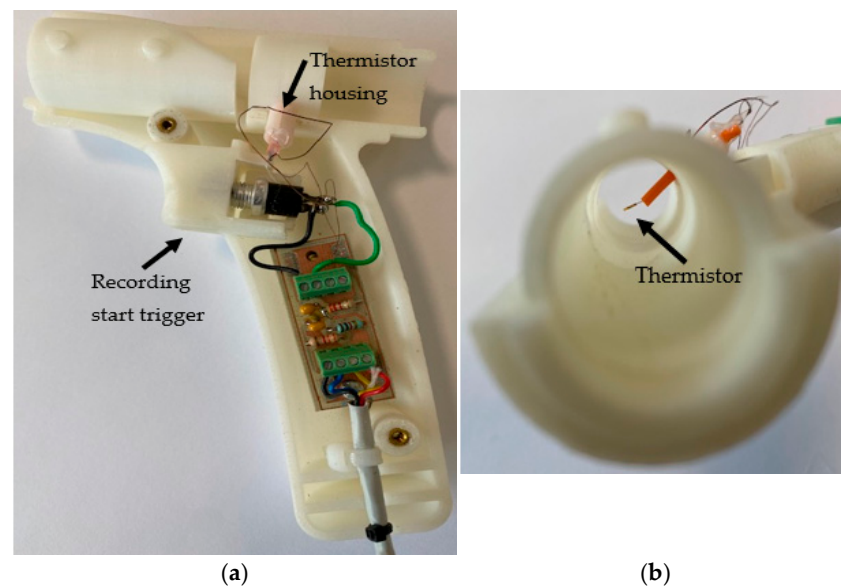


**Figure 4.** (a) The inner parts of the 3D-printed transducer section with the funnel removed. (b) The thermistor location.

Figure 5 shows the transducer section with its funnel removed and the related dimensions in millimeters.

To measure RR, the operator positioned the funnel of the transducer section toward the participant's face and monitored the respiratory signal on the device's screen. The distance of the funnel to the face was typically about 20 cm. The actual distance was established by the operator of the device, ensuring that a respiratory signal was visible on the device's

screen before pressing the start RR measurement trigger mechanism of the device. The device could detect respiratory airflow up to 30 cm from the face in some participants.

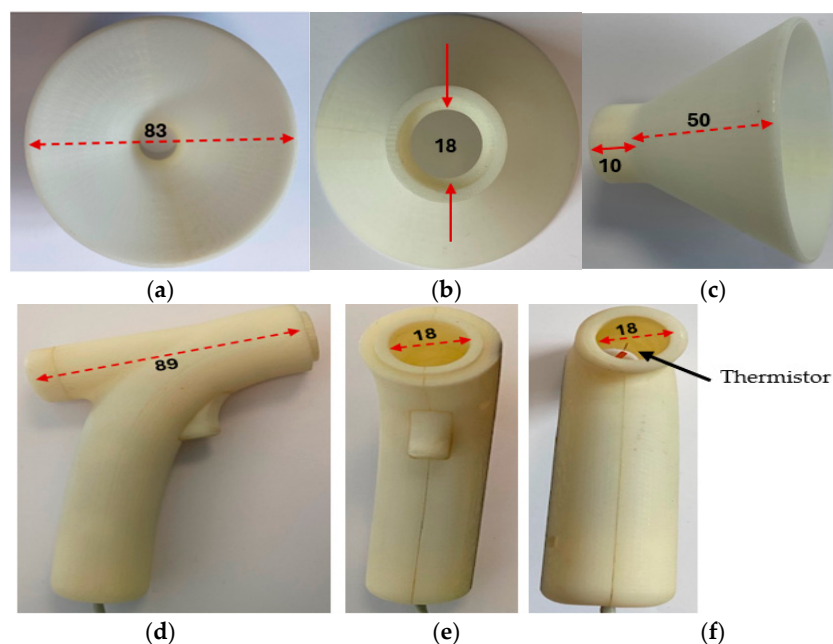


**Figure 5.** The transducer section with its funnel removed and related dimensions shown in millimeters. (a) The funnel air inlet side. (b) The funnel reverse end, the solid red line indicates diameter. (c) The funnel side view. (d) Side view of the transducer section with the funnel removed. (e) Front view of the transducer section with the funnel removed. (f) Reverse view of the transducer section with the funnel removed.

### 3.2. Calculations for the Design Thermistor Circuit and Its Operating Temperature

A self-heating thermistor acted as the sensor to convert respiratory airflow to an electrical signal from which RR was determined. Therefore, its type and design parameters were crucial in the successful operation of the device. In this section, the calculations and simulations undertaken to determine the type and operating parameters of the thermistor are described. The mathematical symbols used in this section and their meanings are included in Table 1.

**Table 1.** List of mathematical symbols for calculations in Section 3.2 and the parameters.

Symbol	Parameter (Unit)
$D_t$	Power dissipation coefficient for thermistor (Watts)
$I_t$	Current through the potential divider (Amp)
$P_t$	Power dissipation in thermistor (Watts)
$R_o$	Resistance of thermistor at temperature $T_o$ ( $\Omega$ )
$R_s$	Potentiometer series resistance ( $\Omega$ )
$R_t$	Resistance of thermistor at temperature $T$ ( $\Omega$ )
$T$	Thermistor temperature (K)
$T_a$	Ambient temperature (K)
$T_o$	Base temperature for thermistor (usually 298 K)
$V$	Velocity of air stream (m/s)
$V_s$	Potentiometer supply voltage (Volts)
$A$	Temperature coefficient of thermistor resistance at temperature $T$ ( $\Omega/^\circ\text{C}$ )
$\beta$	Thermistor constant
$\Delta T$	Thermistor rise in temperature above ambient ( $^\circ\text{C}$ )



### Thermistor Design Assumptions

Some assumptions were required to make the design practical. However, literature searches and discussions with relevant experienced clinicians were carried out to ensure validity of these assumptions. Wherever possible, the related references are included. The respiratory airflow tidal volume is estimated to be 20–500 mL (infants to adults), with respiration rates varying from 6 to 60 bpm, i.e., a period of 1–10 s (corresponding frequency 1–0.1 Hz). The longest time to exhale air is assumed to be half the longest period, i.e., 5 s. Assuming the velocity of the respiratory air during exhalation is constant, the lowest exhale air velocity ( $u$ ) is

$$u = \frac{\text{Lowest tidal volume}}{\text{Largest respiratory orifice area} \times \text{Longest time period}} \quad (1)$$

The point of exhalation could be nasal or oral. Oral exhalation is assumed, since it is the largest area and results in the lowest respiratory airflow velocity. The area is estimated to be about 4 cm<sup>2</sup> maximum (equivalent to a 1.77 cm orifice diameter). So, the lowest velocity is at 6 bpm (i.e., one exhalation cycle every 5 s), and 20 mL per breath through an area of 4 cm<sup>2</sup> results in a minimum estimated exhaled air exit velocity of

$$\text{Minimum estimated velocity} = \frac{20 \times 10^{-6}}{5 \times 4 \times 10^{-4}} = 0.01 \text{ m/s} \quad (2)$$

This velocity value is significantly toward the lower limit, since the lower respiration rates are typically observed in adults who have much larger tidal volumes than children. Although not particularly critical, the maximum respiratory airflow was estimated from maximum adult tidal flow at about 15 bpm (one inhale and one exhale, with each lasting 2 s). Using an orifice of about 2 cm<sup>2</sup>, respiratory airflow velocity is

$$\text{Respiratory air flow velocity} = \frac{500 \times 10^{-6}}{2 \times 2 \times 10^{-4}} = 1.25 \text{ m/s} \quad (3)$$

The exhaled airflow is captured with a funnel, the outlet of which is directed into the device's air chamber containing the self-heating thermistor. The incorporation of the funnel was essential to increase the respiratory airflow catchment area and to allow for any misalignment between the sensing air chamber axis and direction of the respiratory airflow. Various experiments and designs were explored in terms of aesthetic appearance, ease of use, and functionality of the air chamber. The final design had a funnel having an outer diameter of 83 mm feeding into a sensing air chamber that was 89 mm in length and 18 mm in diameter. The length of the air chamber was sufficient to ensure laminar flow for all conditions of use (Reynolds number much less than 2000), and its diameter was sufficiently large to maintain airflow drag to minimum while ensuring that it was maximized in the region of the thermistor sensor. The latter was mounted on the axis of the air chamber approximately halfway along its length. The diffusion between the exit orifice of the exhalation and the funnel and misalignment with the respiratory airflow direction were estimated to reduce the airflow through the air chamber to a conservative 25% of the initial exhaled air velocity, i.e., 2.5 mm/s. In practice, it was found that the actual minimum airflow levels were greater than this by about 50% of the calculated velocity (i.e., 50% of 1.25 m/s = 0.625 m/s) which was also determined by a 2D computational fluid dynamics (CFD) analysis. The requirements for the thermistor sensor then could be specified as follows:

- Respiratory signal frequency range: 0.1–1 Hz.
- Minimum respiratory airflow velocity: 0.005 m/s.

- Maximum respiratory airflow velocity: 0.312 m/s.

### 3.3. Design of Self-Heating Thermistor Sensor Circuit

A negative temperature coefficient (NTC) thermistor, which is a semiconductor-type device whose resistance reduces with temperature increase, was used in the device's design. The thermistor was a self-heating type, where the cooling of the thermistor was a function of the respiratory airflow velocity. The resistance variations were converted to an electrical signal representing respiratory airflow. Compared to typical anemometry applications, the current application required much higher sensitivity and shorter response time. The absolute values of the respiratory airflow velocity were not needed for this design, since the device only required the variations (i.e., rate of change) in the respiratory airflow velocity to determine the value of RR. A potential divider circuit (shown in Figure 6) was used to generate an output voltage signal for the thermistor. The series resistor ( $R_s$ ) limited the current ( $I_t$ ) to the thermistor—represented by its variable resistance as  $R_t$ . The signal from the thermistor ( $V_t$ ) was subsequently band-pass filtered and amplified (explained in following sections). The processes of determining the values  $R_s$  and  $R_t$  are explained in the next sections.

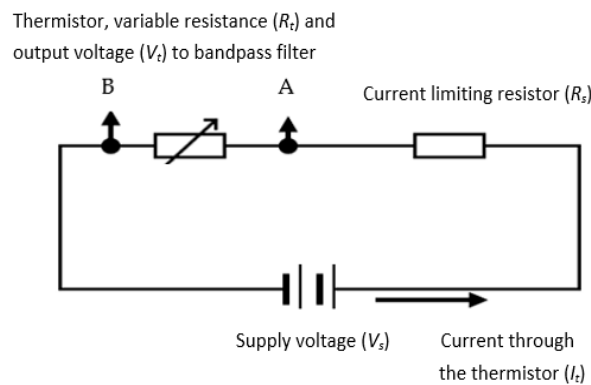


**Figure 6.** The potential divider for the thermistor (A and B are the connection points for the thermistor).

#### 3.3.1. Selection of Thermistor Resistance and Its Series Resistor

The resistance of a thermistor ( $R_t$ ) at a specific temperature ( $T$ ) is expressed as

$$R_t = R_o \times e^{\beta(\frac{1}{T} - \frac{1}{T_o})} \quad (4)$$

where  $R_o$  is the thermistor resistance at temperature  $T_o$ ,  $\beta$  is the thermistor constant [57], and  $R_s$  is the series resistance shown in Figure 6. From this equation, the temperature coefficient ( $\alpha$ ) of resistance at temperature  $T$  for a thermistor is

$$\alpha = \frac{d(R_t)}{d(T)} = -\frac{\beta}{T^2} \quad (5)$$

In this design, to maximize the sensitivity of the thermistor as an air velocity sensor and to ensure detection of the highest respiratory airflow variation frequency, the following parameters required consideration in the design:

- Selection of a thermistor with a high value of  $\beta$ .
- Operation of the self-heating thermistor at a temperature significantly higher than the ambient (room) temperature to maximize the cooling effect due to the respiratory airflow with due regard to the reduction in  $\alpha$  as temperature increases.
- Selection of a thermistor with a low thermal time constant.
- Electrical characteristics compatible with the proposed circuit function.

The design consideration (i) was realized by selecting an appropriate thermistor type. Consideration (ii) was governed by the choice of the thermistor supply volts and potential divider resistance (Figure 6), as explained later. Consideration (iii) required a suitably low impedance output signal but with a low power consumption, and as such, thermistors with  $R_0$  values of 2–10 k $\Omega$  were considered suitable. Consideration (iv) was critical, since if the thermal lag was too long, the higher respiratory frequencies would be heavily attenuated. The thermal lag is linked to thermal capacity and dissipation rate, so it is generally dependent on the shape and size of the thermistor and the lead wire material and gauge. So, a small device with thin leads was best for this application. Ideally, a relatively high dissipation factor is also beneficial, since this would imply a high sensitivity to the cooling by the airflow. Many types of thermistors were commercially available, matching the electrical characteristics, but most had a relatively long thermal lag. Due to the critical nature of this parameter, some preliminary tests were performed on the two most suitable thermistor types having similar electrical characteristics but different thermal lag times and dissipation: (a) the Betatherm Betacurve 3K3A1W2 series and (b) the Measurement Specialties Micro-BetaCHIP 10K3MCD1 thermistor type. Using the circuit shown in Figure 6, the associated tests are described in the next section.

### 3.3.2. Thermistor Time Constant (Thermal Lag)

The thermistor time constant defines the speed at which the thermistor resistance changes when experiencing a change in the surrounding temperature. This is analogous to the time constant of an electrical resistor (R)–capacitor (C) filter. For liquids, this is quoted in data sheets as less than 1 s for the Betacurve device, and for the Micro-Beta device, it is 0.2 s. However, we did not find the required data for air, so tests were carried out to determine its approximate value. To carry out these tests, the supply voltage was applied to the circuit shown in Figure 6, and when stable conditions were reached, a flow of 60 mm/s was switched on (via an electromagnetic valve) for 1 min and then off again, with continuous monitoring of thermistor voltage and current. The thermistor voltage variation with time was exponential, as shown in Figure 7. This was as expected, since the system is analogous to an RC network. The attenuation factor in terms of time constant ( $\tau$ ) is interpreted in Table 2.

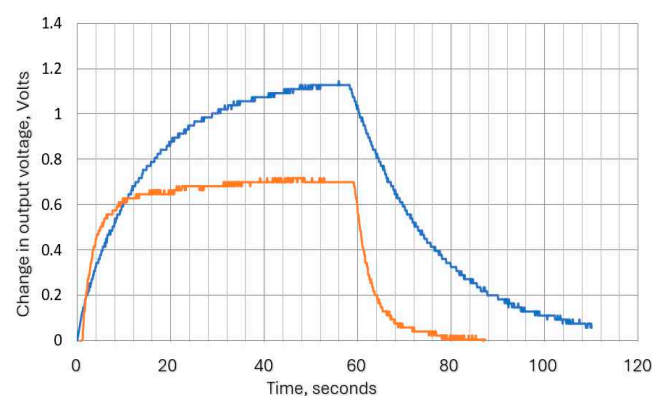


**Figure 7.** Response times for 3K3A1W23k and the 10K3MCD1 10k thermistors (rising edge corresponds to 60 mm/s flow switched on—i.e., cooling phase). Blue plot is for 3 k $\Omega$  thermistor, and orange is for 10 k $\Omega$  thermistor.

The time constants derived from exponential plots in Figure 7 demonstrate that the long thermal lag of the Betacurve device precluded it from use in this application, and no further analysis was carried out for this device.

**Table 2.** The attenuation factor in terms of time constant ( $\tau$ ).

Thermistor Type	Action	Time Constant ( $\tau$ , Seconds)	Attenuation ( $V_{tf}/V_{to}$ ) at 1 Hz (Equivalent to 60 bpm)
Betacurve 3K3A1W2	Power on	20	-
	Flow 0–60 mm/s	12.3	0.0129
	Flow 60–0 mm/s	18.2	0.0087
Micro-BetaCHIP-type 10K3MCD1	Power on	5	-
	Flow 0–60 mm/s	4	0.0398
	Flow 60–0 mm/s	5	0.0318

### 3.3.3. Dissipation Factor ( $D_t$ ) Calculations for the Selected Thermistor

The steady state measurements of thermistor voltage and current obtained from the thermal lag test also enabled the dissipation factor  $D_t$  to be determined for the selected thermistor mounted in the air chamber (the tube containing the thermistor) as follows:

Steady state values were derived as follows:

$$V_t = 7.9 \text{ Volts, } I_t = 1.59 \text{ mA, } T_a = 12^\circ\text{C}$$

$$P_t = V_t \times I_t = 12.56 \text{ mW} \quad (6)$$

$$R_t = \frac{V_t}{I_t} = 4.97 \text{ k}\Omega \quad (7)$$

From the thermistor data sheet, its temperature ( $t$ ) at the resistance value ( $R_t$ ) can be read, allowing the actual dissipation factor  $D_t$  to be determined as follows:

$$D_t = \frac{P_t}{t - T_a} = \frac{12.56 \text{ mW}}{41.5 - 12} = 0.43 \text{ mW}/^\circ\text{C} \quad (8)$$

This test was repeated for the thermistor in free still air and found to also be approximately  $0.43 \text{ mW}/^\circ\text{C}$ . In the data sheet, the still air value for  $D_t$  is quoted to be  $0.3 \text{ mW}/^\circ\text{C}$ . Since the precise conditions used for obtaining this value were not described, the difference may be due to conduction through the connecting leads.

### 3.3.4. Thermistor Operating Temperature Calculations

The thermistor operating temperature needs to be at high enough to give a large change in resistance ( $\Delta R_t$ ) with the respiratory airflow velocity ( $u$ ), i.e.,  $\frac{d(R_t)}{d(u)}$  needs to be a maximum. The cooling effect of the air stream and thus the temperature of the thermistor are directly proportional to the difference between  $T$  and ambient (room) temperature:

$$\frac{d(T)}{d(u)} = C(T - T_a) \quad (9)$$

where  $C$  is a cooling constant, and  $T_a$  is ambient temperature. As

$$\frac{d(R_t)}{d(T)} = \frac{-\beta}{T^2} \quad (10)$$

we can write

$$\frac{d(R_t)}{d(v)} = \frac{d(R_t)}{d(T)} \times \frac{d(T)}{d(v)} = \frac{-\beta}{T^2} C(T - T_a) \quad (11)$$

Differentiating this with respect to  $T$  allows the maximum conditions for  $\frac{d(R_t)}{d(T)}$  to be defined as

$$\frac{\beta}{T^3} C(T - 2T_a) = 0 \quad (12)$$

i.e., the running temperature  $T = 2 \times$  ambient temperature  $T_a$ . This is well above a desirable operating temperature and exceeds the limiting conditions for the thermistor, but it does confirm that the sensitivity increases with usable ranges of  $T$ . Thermistors are semiconductor-like devices and are easily damaged when operated above their manufacturers' stated maximum temperature ratings. For this application, the maximum ambient temperature was estimated to be 35 °C. The minimum working temperature range for a typical thermistor is about −20 °C to 105 °C. The lower temperature limit will not be a limitation, but it is important not to exceed the upper temperature limit. Allowing a safety margin of 25%, the upper temperature limit is about 75 °C. Ambient temperature is specified to be 10 °C to 35 °C. So, the self-heating of the thermistor must not increase its temperature by more than about 40 °C maximum. A rise of 35 °C was eventually chosen such that the 'at rest' temperature of the thermistor would not exceed 70 °C to avoid possible damage to the heat chamber (sensing tube) and the thermistor supporting components.

### 3.3.5. Selection of Supply Voltage and Potential Divider Series Resistance Values

In this section, the supply voltage ( $V_s$ ) and the potential divider series resistance ( $R_s$ ) values are determined.

**Supply Voltage ( $V_s$ ):** A conventional low-cost 12-volt rechargeable lead acid battery (as described in the following sections) was selected for  $V_s$ , since this suited the power requirements for any LED or similar device that might be used as embellishments that might be added to the device in the future. Depending on the state of charge, the actual battery can vary from around 11.5 to 14.7 volts, so a value of 13 volts was used in the calculations to determine the value of  $R_s$ .

**Series Resistor ( $R_s$ ):** In a potential divider such as the one shown in Figure 5, the output thermistor voltage ( $V_t$ ) is given by

$$V_t = \frac{V_s \times R_t}{R_s + R_t} \quad (13)$$

For the greatest sensitivity value, the variation in  $V_t$  with  $R_t$  needs to be maximized, i.e.,

$$\frac{dV_t}{dR_t} = \frac{V_s \times R_s}{(R_s + R_t)^2} \quad (14)$$

The parameter  $\frac{dV_t}{dR_t}$  is at a maximum when  $R_t = R_s$ . This equivalence cannot be maintained under all conditions due to the variation in  $R_t$  with temperature, so the aim should be for an  $R_s$  value that is in the region of the range of the  $R_t$  values expected through the working temperature range.

**Optimum value for ( $R_s$ ):** Although, as shown above,  $R_s = R_t$  for maximum sensitivity, the chosen  $R_s$  value must also ensure that the thermistor runs within the selected operating temperature range. The temperature rise,  $\Delta T$  (in °C), of the thermistor due to self-heating is given by

$$\Delta T = \frac{P_t}{D_t} = (T - T_a) \quad (15)$$

where  $P_t$  is the power dissipation in the thermistor given in watts (W), and  $D_t$  is the thermistor dissipation coefficient given in W/°C. For a potential divider circuit shown in Figure 6, the current,  $I_t$ , flowing through it is

$$I_t = \frac{V_s}{R_t + R_s} \quad (16)$$



where  $V_s$  is the potential divider supply voltage, and  $R_s$  is the series resistor. The power dissipated by the thermistor  $P_t$  is

$$P_t = I_t^2 R_t = \left( \frac{V_s}{R_t + R_s} \right)^2 R_t \quad (17)$$

From Equations (14)–(16),

$$\Delta T = (T - T_a) = \left( \frac{V_s}{R_t + R_s} \right)^2 \times \frac{R_t}{D_t} \quad (18)$$

Solving for positive values of  $R_s$  from Equation (17),

$$R_s = \frac{2}{2D_t(T - T_a)} \left( D_t \times R_t \times (T_a - T) + V_s \times (D_t \times R_t \times (T - T_a))^{0.5} \right) \quad (19)$$

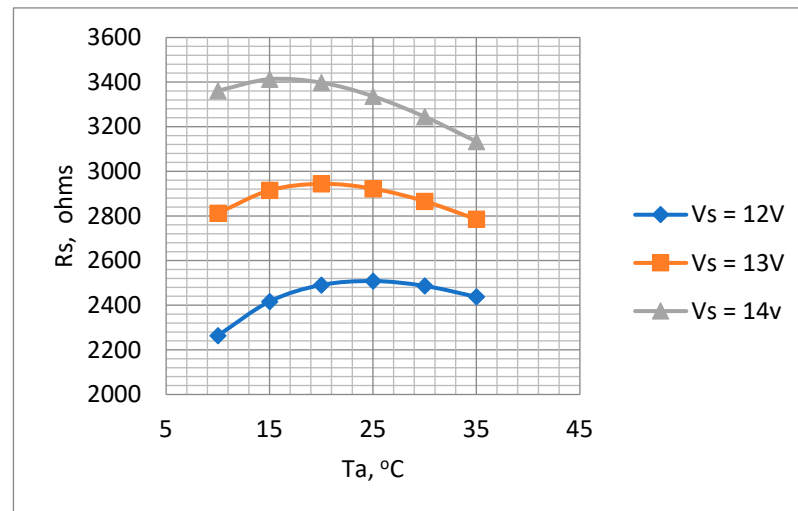
where

$$R_t = R_o \times e^{\beta \left( \frac{1}{T} - \frac{1}{T_o} \right)} \quad (20)$$

In Equation (19), for a given thermistor, the variables are  $T_a$  and  $V_s$ , so the equation provides a valuable guide as to the suitable  $R_s$  values required to achieve the designed temperature rise  $(T - T_a)$  over the possible range of battery voltages. The values indicated below correspond to the Micro-BetaCHIP-type 10K3MCD1 thermistor:

- Thermistor parameter  $\beta = 3976$ .
- $D_t = 0.413 \text{ mW}/^\circ\text{C}$  (see Section 3.3.3).
- $T_o = 298 \text{ K}$ .
- $V_s = 12\text{--}14 \text{ V}$ .
- $T - T_a = 35^\circ\text{C}$ .

The plots for  $T_a = 10^\circ\text{C}$  to  $35^\circ\text{C}$  are shown in Figure 8.



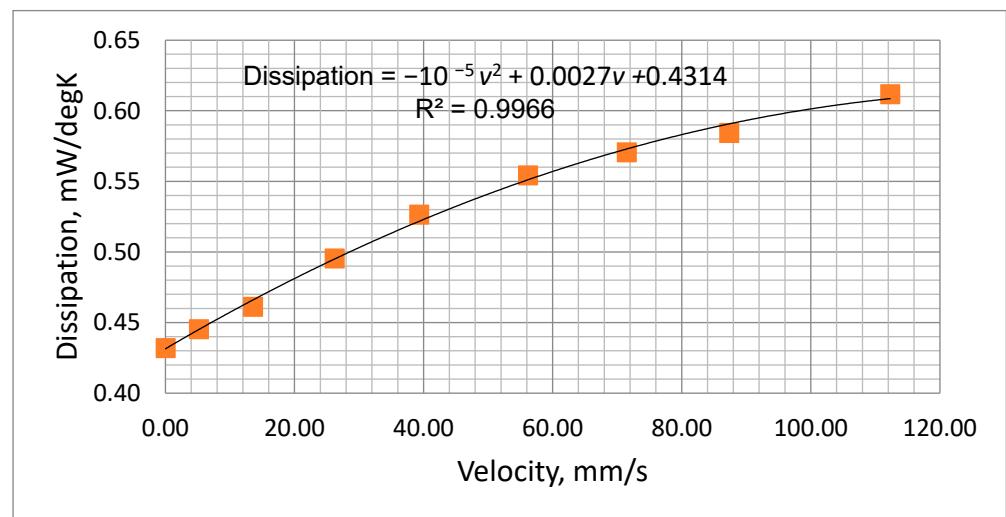
**Figure 8.** Variations in  $R_s$  with  $T_a$  for supply voltages 12 V, 13 V, and 14 V.  $R_o = 10 \text{ k}\Omega$  to determine optimum  $R_s$  value.

Figure 8 indicates that the values of  $R_s$  ranged between 2.3 k $\Omega$  to 3.4 k $\Omega$  depending on ambient temperature and battery voltage. A value of 3.3 k $\Omega$  was selected for  $R_s$ . Although this value of  $R_s$  is higher than the ideal for the lower battery voltages, it nevertheless ensures that the temperature will not rise to an unacceptable level when the battery is fully charged. The suitability of this value was checked by a test of the thermistor mounted in the air chamber with the chosen values of  $R_s$  and the voltage across it, i.e.,  $V_s$ . As

described previously (Section 3.3.3) by measuring the thermistor voltage ( $V_t$ ) and current ( $I_t$ ) (Figure 6), both its temperature and dissipation rate could be determined for various values of flow rate. The results obtained are presented in Table 3 and Figure 9, which show the measured dissipation rate variations with airflow velocity. These indicate a reduction in sensitivity as the cooling airflow velocity increased. This is as expected, since as the airflow velocity increases, the thermistor temperature decreases, thus reducing its temperature differential with respect to the ambient temperature.

**Table 3.** Measured values of  $D_t$  at various airflow rates.

Velocity mm/s	$V_s$ (Volts)	$T_a$ (°C)	$V_t$ (Volts)	$I_t$ (mA)	$P_{t_r} = V_t \times I_t$ (mW)	$R_t = V_t/I_t$ (kΩ)	Temperature (°C) (Data Sheet)	$D_t$ (mW/K)	$\Delta D_t$ (mW/K)
0.0	13	11.8	8.02	1.53	12.27	5.24	40.20	0.43	0.00
5.2	13	12.6	8.03	1.52	12.21	5.28	40.00	0.45	0.01
13.6	13	12.6	8.19	1.47	12.04	5.57	38.70	0.46	0.03
26.2	13	12.6	8.51	1.38	11.74	6.17	36.30	0.50	0.06
39.3	13	12.6	8.75	1.3	11.38	6.73	34.20	0.53	0.09
56.1	13	12.4	8.97	1.23	11.03	7.29	32.30	0.55	0.12
71.5	13	12	9.14	1.18	10.79	7.75	30.90	0.57	0.14
87.3	13	12	9.22	1.16	10.70	7.95	30.30	0.58	0.15
112.3	13	11.9	9.37	1.11	10.40	8.44	28.90	0.61	0.18



**Figure 9.** Measured power dissipation variation with airflow velocity.

The plot of Figure 9 was fitted to a second-order polynomial which could be used to predict the thermistor dissipation factor ( $D$ , mW/°C) at various airflow velocities ( $v$ , mm/s), i.e.,

$$D = -10^{-5} v^2 + 0.0027v + 0.4314 \quad (21)$$

### 3.3.6. Calculation of Estimated Sensitivity with the Selected Thermistor and $R_s$ Value

It was considered valuable to develop a method of predicting the results of Table 3, since it would allow for the performance of different thermistors and associated components

to be assessed without the need for practical measurements. It would also allow for checking the results at different ambient temperatures. Solving Equation (19) for  $D_t$ ,

$$D_t = V_s^2 \frac{R_t}{\Delta T (R_t^2 + 2R_t \times R_s + R_s^2)} \quad (22)$$

where

$$R_t = R_0 \times e^{\beta(\frac{1}{T_a + \Delta T} - \frac{1}{T_0})} \quad (23)$$

Substituting  $R_t$  from Equation (23) into Equation (13) allows the output voltage,  $V_t$ , versus temperature rise ( $\Delta T$ ) to be determined, and Equation (20) defines the power dissipation,  $D_t$ , versus temperature rise ( $\Delta T$ ). Using data from these equations, it was possible to plot estimated the thermistor output voltage,  $V_t$ , as a function of the power dissipation,  $D_t$  (Figure 10). The results corresponded well with the measured values. The results are valuable because power dissipation is directly related to the cooling effect of the respiratory airflow, and thus, Figure 10 indicates the predicted overall sensitivity.

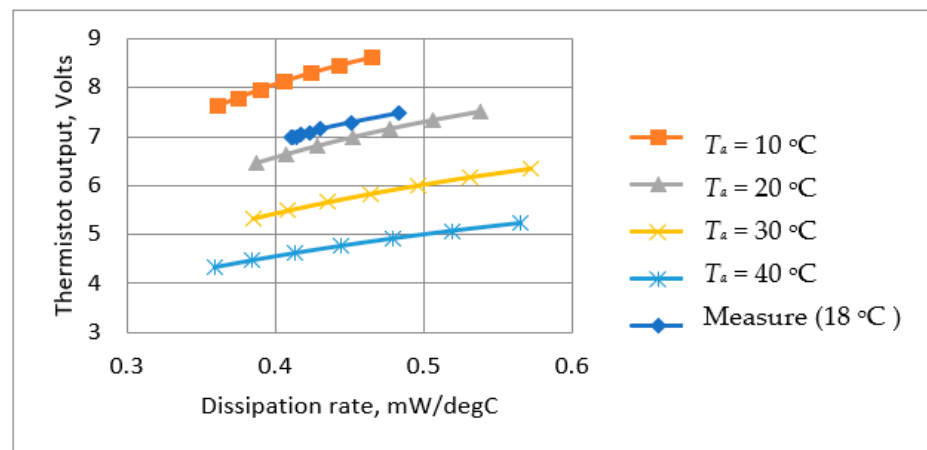


**Figure 10.** Calculated and measured steady thermistor output voltage as a function of power dissipation at different ambient temperatures.

### 3.3.7. Thermistor Output Voltage Measurements at Different Respiration Rates and Flow Velocities

Tests were carried out to ensure that the attenuation due to the thermistor time constant did not reduce the thermistor output signal amplitude to unacceptable levels. To enable the signal to be magnified, the steady state (zero airflow) DC (direct current) thermistor voltage was balanced out, so the figures show the voltage change when the airflow was switched on. Figure 11 shows two such traces, with the remaining results summarized in Figure 12. The actual minimum and maximum values were 0.02 volts and 0.71 volts, respectively.

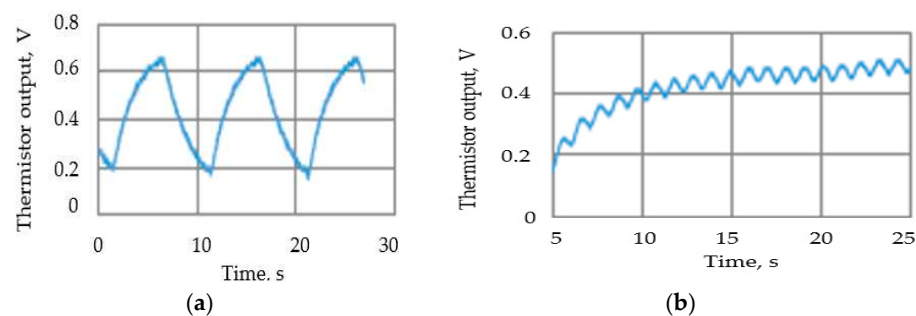


**Figure 11.** Examples of the thermistor ( $V_t$ ) output voltage traces: (a) airflow velocity = 63 mm/s, 10 s cycle; (b) airflow velocity = 63 mm/s, 1 s cycle.

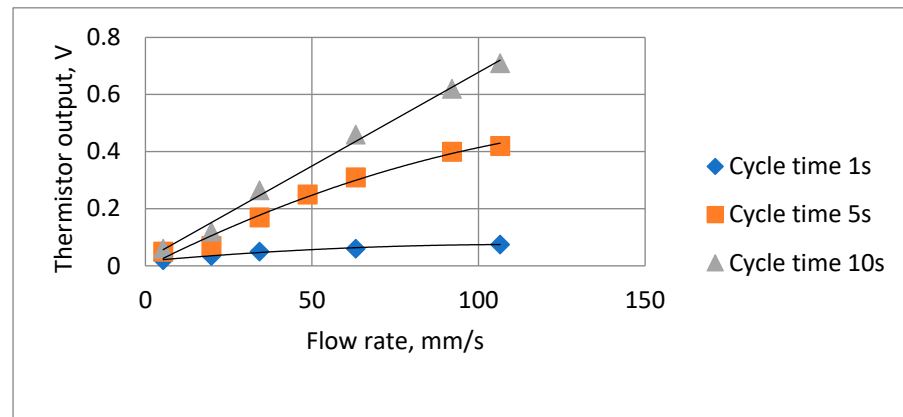


**Figure 12.** Summary of thermistor output voltage amplitudes at different cycle times and flow rates.

### 3.3.8. Theoretical Relationship Between Respiratory Airflow Velocity and Power Dissipation Rate

The relationship between thermistor power dissipation rate,  $D_t$ , and the respiratory airflow velocity is complex and depends on the Prandtl, Nusselt, and Reynolds numbers [58], which are in turn related to the physical parameters and the velocity distribution of the air stream and the shape and size of the thermistor. Studies have investigated cooling effects such as this and have developed empirical formulae to enable theoretical predictions of cooling rates, but all tend to be specific to the particular characteristics of the test arrangement. Since the thermistor output response versus airflow rate fitted well to a second-order polynomial over the range of interest for this device, it was not considered useful to go through the process of adapting the published formulae.

## 3.4. Description of Device's Electronic Circuitry

In this section, the design of the device's electronic circuitry is described.

### 3.4.1. Signal Conditioning Circuit

The thermistor signal was fed via a cable to a pre-amplifier circuit in the base unit section of the device (shown in Figure 1). The circuit used an OP200 dual low offset, low-power operational amplifier [59]. It consisted of a high-pass filter that ensured that the “at rest” direct current (DC) voltage component from the potential divider was blocked from the amplifier input. The thermistor amplification circuit is shown in Figure 13.

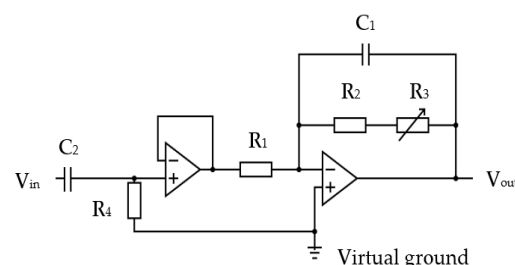


**Figure 13.** The thermistor signal amplification circuit:  $R_1 = 10 \text{ k}\Omega$ ,  $C_2 = 2200 \text{ nF}$ ,  $R_4 = 220 \text{ k}\Omega$ ,  $R_1 = 10 \text{ k}\Omega$ ,  $R_2 = 50 \text{ k}\Omega$ ,  $R_3 = 200 \text{ k}\Omega$  variable,  $C_1 = 220 \text{ nF}$ .

The inherent thermal lag of the thermistor provided an adequate low-pass filtering to remove any spurious pulse signals arising from sudden changes in airflow velocity, e.g., airflow changes from the recording room air conditioning, among others. However, an additional electronic low-pass filter circuit was included to remove any higher electromagnetic frequencies that might be picked up by the circuit. Two amplifier stages were adapted,

with the first being a simple voltage follower that provided a consistent high-impedance load for the thermistor circuit. The second stage had an adjustable gain (through  $R_3$  variable resistor) to allow the circuit gain to be trimmed during its testing. The second stage also provided the additional filtering for spurious high-frequency noise. The operational amplifiers were supplied with a 3.3 V power source via a voltage stabilizer (discussed in following sections). This voltage level ensured compatibility with the microcontroller input. The amplified thermistor signal was digitized by the microcontroller's analogue-to-digital convertor (ADC, 10-bit resolution).

### 3.4.2. Microcontroller

STM32F407 Discovery board device [60], shown in Figure 14a, was used for the device to control the respiration rate measurement, perform required operations, and display the relevant information on the device's display unit. Its LCD display [61] is shown in Figure 14b.

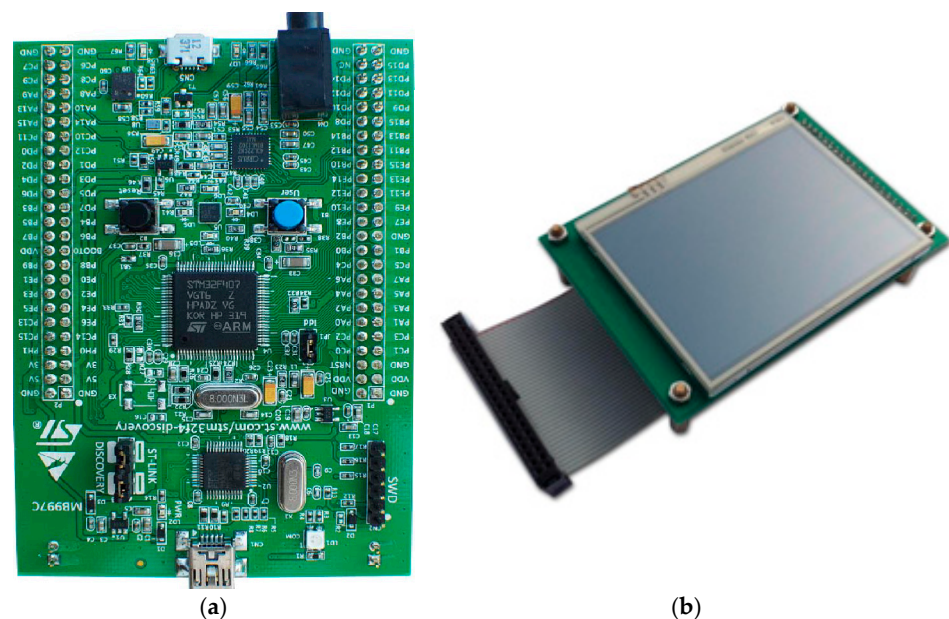


**Figure 14.** (a) STM32F407 VGT6 Discovery microcontroller used for the device [60], (b) STM32F4DIS-LCD [61].

This microcontroller is designed for industrial and consumer applications, utilizing 32-bit Arm® Cortex®-M4 with floating-point unit (FPU) core, 1 Mbyte flash memory and 192-Kbyte random-access memory (RAM) (STM Microelectronics). It provides low power consumption, high performance, and ease of use with developing applications. With its 32-bit microprocessor, it supports digital signal processing instructions and a wide range of standard communication protocols. It is compatible with multiple Integrated Development Environments (IDEs), such as Keil MDK-ARM. The microcontroller was connected to an STM32F4DIS-LCD [61] (shown in Figure 14b) to allow the respiratory signal and RR rate to be displayed.

### 3.4.3. Recording Start Trigger Mechanism Circuit

The start RR measurement trigger mechanism was integrated into the transducer part (section A) of CPRM. Its circuit is shown in Figure 15. It incorporates a 4N25 optocoupler (manufacturer: Vishay Semiconductors) [62] with a 1 k $\Omega$  resistor at its input and 10 k $\Omega$  pull-up resistor connected to regulated 3.3 volts ( $V_{cc}$ ).



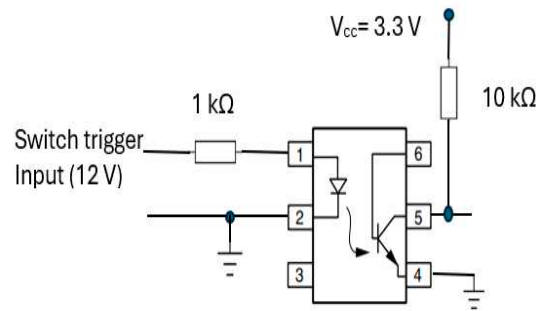


**Figure 15.** Optocoupler (4N25) [62] circuit for start recording trigger mechanism.

This optocoupler is an industry standard dual-in-line 6-pin package. Its incorporation ensured isolation of the operator of the device from the electrical circuitry. By pressing the trigger mechanism, the device's output pin (i.e., pin 5) goes high (i.e., to the supply voltage,  $V_{cc}$ ). As the device's output is connected to an input port of the microcontroller, a change in voltage level would indicate the start of RR measurement.

#### 3.4.4. Buzzer Mechanism Circuit

The buzzer mechanism was incorporated into the device's base unit section to indicate completion of RR measurement, allowing the operator of the device to read the measurement. Its circuit (shown in Figure 16) consisted of an IRF530 (N-channel) MOSFET [63] that is designed for fast switching and requires a simple drive circuit. Its resistance is  $0.16\ \Omega$  and can operate from  $-55\ ^\circ\text{C}$  to  $+175\ ^\circ\text{C}$ . The gate input pin of IRF530 was connected to an output pin of the microcontroller. Its input pin was raised to 'high' for a second to activate the buzzer.

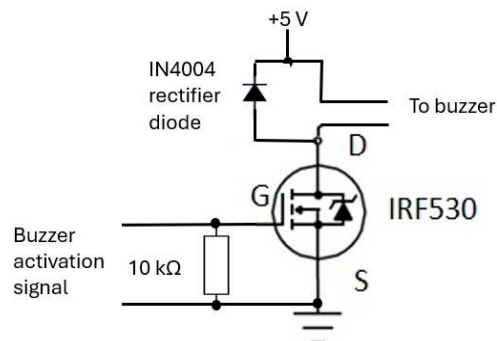


**Figure 16.** The buzzer circuit alerts the operator to read the RR value from CPRM display.

#### 3.4.5. Regulated Power Supply Circuit

The power supply elements of the device consisted of a 12 V, rechargeable, sealed lead acid, 0.8Ah, YUCEL battery [64] (Figure 17a). The battery was housed in CPRM base unit with an external port to connect its charger. Its charger was an Ansmann ALCS 2-24A [65] (Figure 17b). There were two voltage regulators: one providing 5 V (Figure 17c) and the other providing 3.3 V (Figure 17d). The 5 V regulator circuit incorporated a 7805T [66] device that is commonly used in electronic circuits to provide a constant +5 volts output for a variable (unregulated) input supply voltage. Its minimum and maximum input voltages are 7 V and 25 V, respectively. Its operating current is 5 mA. A 3.3 V regulator circuit was incorporated [67] into the device.

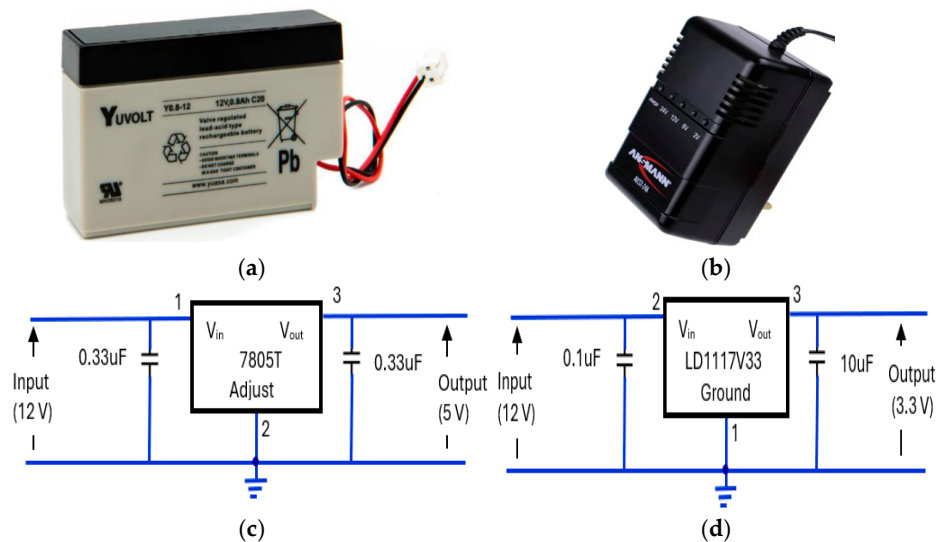


**Figure 17.** The elements of the device's power supply unit: (a) 12 V rechargeable battery [64], (b) battery charger unit [65], (c) 7805T [66] regulator for 5 V supply, (d) LD1117V33 [67] regulator for 3.3 V supply.

### 3.5. Description of the Device's Software

In this section, the method of determining RR from the recorded respiratory signal and other aspects of CPRM's software are explained. CPRM uses a signal sample rate of 20 samples per second to record the respiratory signal. The signal was stored on the STM32F407 VGT6 Discovery microcontroller [60] memory storage. Given that the respiratory signal was unlikely to exceed 60 bpm or 1 Hz, 20 sample per second was adequate. The software was set up to capture 1024 samples (data points). This corresponded to a recording duration of  $1024/20 = 51.2$  s. To determine RR, the fast Fourier transform (FFT) operation was prepared in C language and integrated into the microcontroller. Using the FFT function, the magnitude frequency spectrum of the recorded respiratory signal was obtained by determining absolute (magnitude) values of the resulting discrete Fourier transform complex numbers. A requirement for FFT operation is that the number of data points ( $N$ ) needs to conform to  $2^k$ , where  $k$  is an integer number. In our work,  $k = 10$ , resulting in 1024 samples. The frequency resolution provided by 1024 data points was calculated by dividing the sample rate by the total data points, i.e.,  $20/1024 = 0.0195$  Hz. This frequency resolution corresponds to RR resolution of  $0.0195 \times 60$ , i.e., about 1 bpm. Reducing the number of recorded sample points negatively affects the RR resolution (accuracy of measuring RR), and increasing the number of samples results in a longer measurement time (this issue is discussed further in the Discussions section). CPRM used the frequency corresponding to the highest peak in the magnitude frequency spectrum to determine RR (i.e.,  $RR \text{ in bpm} = \text{frequency associated with the highest peak} \times 60$ ).

As part of evaluating CPRM (details included in the next section), its measurements were compared with a commercially available respiration monitor, SOMNOtouch™ RESP [15]. This device does not indicate RR, but it can record respiratory signals from two bands—one wrapped around the chest and the other around the abdomen. These signals were averaged to determine an overall respiratory effort. A typical respiratory signal recorded using SOMNOtouch™ RESP is provided in Figure 18. Its magnitude frequency spectrum, with the frequency associated with the highest peak = 0.269 Hz, is also shown in the figure. This frequency corresponds to an RR of  $0.269 \times 60 = 16.1$  bpm.

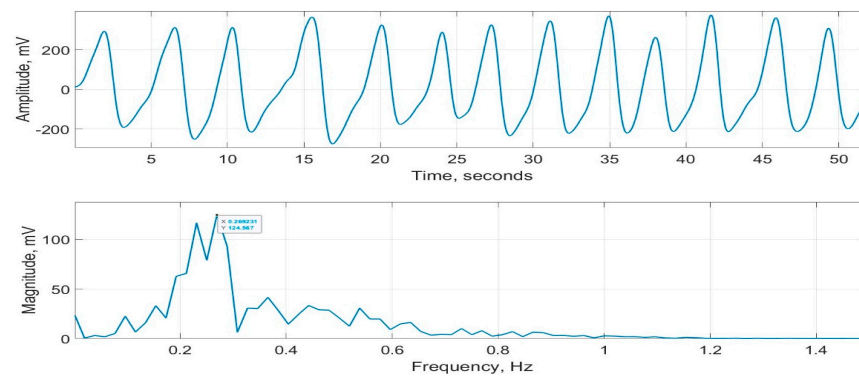


**Figure 18.** Respiration signal recorded using SOMNOtouch™ RESP (**top figure**) and its magnitude frequency spectrum (**bottom figure**).

The microcontroller code was based around a state machine approach for the user interface and display updates. A hardware-based timer interrupt and the microcontroller's onboard 12-bit analogue-to-digital converter in Direct Memory Access mode were used to ensure that timing and data acquisition were accurate, as required for the subsequent software based FFT operation. The start of the measurement cycle was controlled by the device trigger button connected to an external interrupt pin on the microcontroller.

### 3.6. CPRM Evaluation Procedure

The evaluation of CPRM in the current study involved 27 healthy adult volunteers; however, CPRM has also been previously evaluated on children (details of this evaluation are included in the Discussions section). The ethical approval for the study was granted by the UK's National Health Service (NHS reference number SCH/13/018, correspondence reference 149145). The participants were provided with the study's information sheet that outlined the details of the study, their rights, and the means of data handling. The participants signed a consent form agreeing to take part in the study. The mean and standard deviation of their ages were 32.8 years and 8.6 years, respectively (minimum and maximum: 20 years and 52 years, respectively). The participants were 9 males and 18 females.

The participants sat in a comfortable chair and were asked to relax and breathe normally. For comparison to CPRM, the inductance plethysmography was performed using SOMNOtouch™ RESP device. The recording room temperature was around 22 °C. Two experienced clinicians (about 30 and 10 years related clinical experience) were simultaneously involved with each experiment. A clinician operated the CPRM device, and another visually determined the RR by counting chest movement of the participant while the participant wore the SOMNOtouch™ RESP device. The two clinicians performed their measurements independently to ensure that the RR values were not biased by the RR reading of another method. The RR measurements from the three methods (visual counting of the chest movement, SOMNOtouch™ RESP, and CPRM) were simultaneous. The monitoring duration for all three methods was the same allowing consistency in the measurements. For each participant, the experiment was repeated four times, and the results were averaged. Statistical mean values, scatter plots, and box plots were used to compare the RRs obtained for the three methods.

## 4. Results

The means and the standard deviations of the measured RRs by the CPRM, visual counting of chest movement, and SOMNOtouch™ RESP are shown in Table 4. The mean RR values ranged from 13.1 bpm for the visual counting method (lowest value) to 14.6 bpm

(highest value) for the CPRM. The highest RR variability (5.5 bpm) across the participants (measured by the standard deviation) was associated with the SOMNOtouch™ RESP device.

**Table 4.** Mean and standard deviation of respiration rates determined by the three methods.

Respiration Measurement Method	Mean Respiration Rate (bpm)	Standard Deviation of Respiration Rate (bpm)
CPRM	14.6	5.0
Visual counting of chest movement	13.1	4.8
SOMNOtouch™ RESP	14.0	5.5

The percentage differences (shown in Table 5) between the RRs measured using the three methods were lowest for the CPRM and SOMNOtouch™ RESP, i.e., 3.8%. The difference was highest between the CRRM and visual counting, i.e., 11.0%.

**Table 5.** Percentage difference between respiration rates measured by the three methods.

Respiration Measurement Method	Percentage Difference in Means (bpm)	Percentage Difference in Standard Deviations (bpm)
CPRM versus Visual	11.0%	3.4%
SOMNOtouch™ RESP versus Visual	6.7%	10.4%
CPRM versus SOMNOtouch™ RESP	3.8%	−6.9%

Conformance to normal distribution for the RR measure was examined using the Shapiro–Wilk test, and none of the measures conformed to the normal distribution (i.e.,  $p = 000$ , to 3 decimal places). Therefore, to analyze the correlation between the RR obtained using the three methods, Spearman’s rank correlation was adapted, as it is more suited to non-normally distributed data compared to Pearson’s correlation. The resulting correlation matrix is provided in Table 6. The highest correlation (i.e., 0.900) was between the CPRM and SOMNOtouch™ RESP, and the lowest (i.e., 0.892) was between the visual counting of chest movement method and the CPRM.

**Table 6.** Correlation coefficients matrix for respiration rates obtained using the three methods.

Respiration Measurement Method	CPRM	Visual	SOMNOtouch™ RESP
CPRM	1.000	0.892	0.900
Visual counting of chest movement	0.892	1.000	0.985
SOMNOtouch™ RESP	0.900	0.985	1.000

The scatter plots of the RR measurements using the three methods are shown in Figures 19–21. The best straight-line fit is shown in red. The methods provided a close relationship; however, two outliers are visible in the plots.

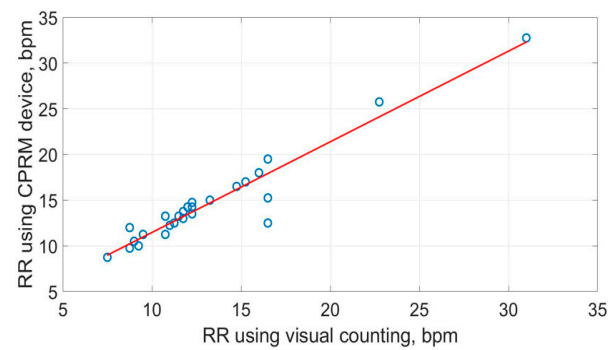


**Figure 19.** Scatter plot of respiration rate measured by CPRM against the visual chest movement counting method.

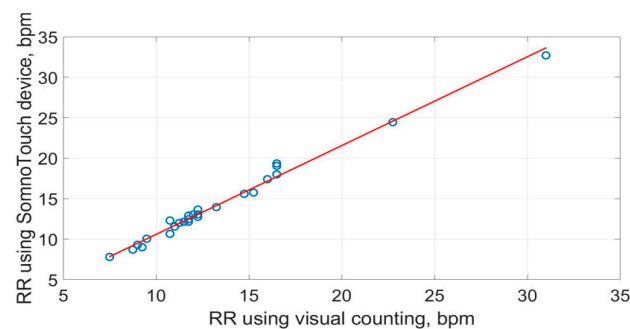


**Figure 20.** Scatter plot of respiration rate measured by SOMNOtouch™ RESP against the visual counting of chest movement.

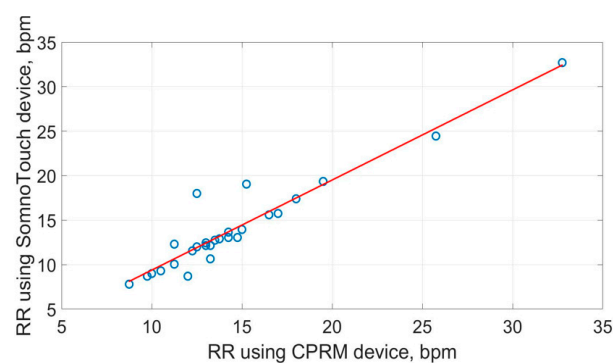


**Figure 21.** Scatter plot of respiration rate measured by CPRM against SOMNOtouch™ RESP.

The box plots comparing the RR measurements using the three approaches are provided in Figure 22. The red line inside each boxplot is the measurement median, which is close for all three approaches.

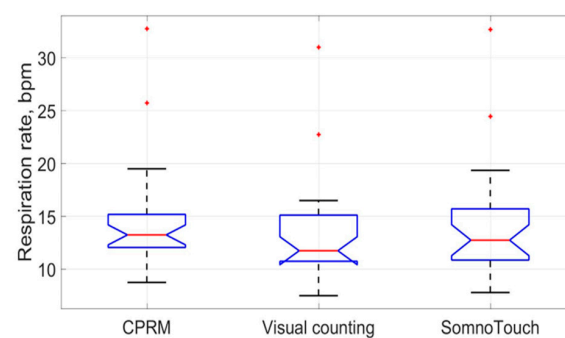


**Figure 22.** Box plots of the three respiration rate methods (the red lines indicate median values).



## 5. Discussions

The design and evaluation of the CPRM device as a new noncontact, cost-effective, and easy-to-use RR measurement device were described. The device operates by detecting respiratory airflow using a self-heating thermistor. This provided a sensitive and sufficiently fast response to variations in respiratory airflow and coped well with a broad range of RR values. The device's hardware provided the required signal conditioning to ensure accurate noise removal and digitization. The optimal operational parameters of the self-heating thermistor for RR measurement were determined through careful design and simulations. The features of the microcontroller provided an effective means of determining RR. The device's display unit shows the respiratory signal in real time, the RR rate (after completion of measurement), and the timing information (i.e., count down of time, in seconds, from when the measurement started to the end of measurement). Once the measurement is complete, the RR value is displayed on the device's screen, and the operator is alerted by a buzzer to read the value from the display.

In this study, the CPRM was evaluated on 27 healthy adult volunteers with simultaneous RR measurements of chest movement visual counting and the SOMNOtouch™ RESP device. To determine the RR using the SOMNOtouch™ RESP device, its recorded respiratory signal was processed using fast Fourier transformed offline, and the frequency associated with the highest peak in its magnitude frequency spectrum was identified and multiplied by 60 (providing the RR in bpm). The RR values obtained simultaneously using the three methods were close; however, the mean RR for chest movement visual counting method was 11% lower than the RR from the CPRM, i.e., 13.1 bpm for visual counting against 14.6 bpm for the CPRM (i.e., difference of 1.5 bpm). The mean percentage difference between the RR measured by the CPRM and that determined from the SOMNOtouch™ RESP was 3.8%, or 0.6 bpm. The difference was lower than the difference between the RR measurements obtained by the CPRM and visual counting of chest movement.

The visual counting method is the “usual care” method that is used routinely in clinical practice but is known to have low interobserver reliability (subjective measurement) [10]. The SOMNOtouch™ RESP device was adapted for an objective measurement comparison with the CPRM.

The evaluation of the CPRM reported in this study focused on healthy adult volunteers. However, in our earlier study, we also evaluated the CPRM on 30 children (aged 8 months to 15 years) at Sheffield Children's Hospital (Sheffield, UK) [9]. The measurements were simultaneously obtained from respiratory inductance plethysmography bands, visual counting of chest movements, and the CPRM. The results showed substantial agreement between measurements from the CPRM and the RIP (interclass correlation coefficient; 0.762; 95% CI 0.633–0.850). When the measurements from two of the children with significantly dysfunctional breathing were excluded, the CPRM showed a much higher correlation with the RIP method (interclass correlation coefficient: 0.981; 95% CI 0.968–0.989), with 95% limits of agreement found at −2.49–0.77 breaths/min.

The future direction of the work include the following:

- **Miniaturization of the device:** Currently, the CPRM uses a base unit with dimension length = 24 cm, width = 16 cm, and height = 9 cm. However, it is possible to replace the current microcontroller board with a more dedicated microprocessor-integrated circuit and use surface mount electronic components, thus reducing the device's size. Its rechargeable battery can also be replaced with a smaller type.
- **RR recording time:** Currently, 1024 samples (data points) were recorded at 20 samples per second. This corresponds to a recording duration of  $1024/20 = 51.2$  s. In the follow-up model of the device, the recording duration will become adaptive, allowing a lower recording duration for babies and young children (who have higher respiration

rates compared to adults) that may not cooperate and a higher recording duration for adults that have a much lower respiration rate and are more cooperative. This would require an alternative means of determining the RR from the respiratory signal, e.g., breath-by-breath RR calculation, whereby the time between successive respiratory cycles is measured [27].

- The CPRM will be further evaluated in clinical settings on a larger population of varied age groups. This would allow more substantial statistical analysis.
- We will ensure full conformance with the medical devices directives (MHRA) [68] to allow its routine clinical use.

## 6. Conclusions

The hardware and software designs and development of a new noncontact respiration rate (RR) monitor utilizing a self-heating thermistor were described. The process of designing the parameters of the self-heating thermistor was outlined. The device (CPRM) facilitates RR measurement objectively compared to the subjective visual chest movement counting method that relies on the experience and level of attention of the clinician. The RR measured by the CPRM was close to that obtained from a commercial device called SOMNOtouch™ RESP. The CPRM is easy to operate, cost-effective, and robust in its functioning.

**Author Contributions:** All authors have contributed to conceptualization, methodology, software, validation, formal analysis, resources, data curation, writing—original draft preparation, writing—review and editing, visualization; supervision, project administration and funding acquisition. All authors have read and agreed to the published version of the manuscript.

**Funding:** This research was funded by the National Institute of Health Research (NIHR), United Kingdom, scheme Invention for Innovation (i4i), Reference: II-LB-0712-20004.

**Institutional Review Board Statement:** The study was conducted in accordance with the Declaration of Helsinki and approved by the UK's National Health Service (NHS reference number SCH/13/018; correspondence reference 149145). The approval date was 27 January 2015.

**Informed Consent Statement:** Informed consent was obtained from all subjects involved in the study.

**Data Availability Statement:** The original contributions presented in this study are included in the article material. Further inquiries can be directed to the corresponding author.

**Acknowledgments:** This work was made possible by the kind participation of the individuals taking part in evaluating the device. The authors are very grateful for their assistance.

**Conflicts of Interest:** The authors declare no conflicts of interest.

## Appendix A

**Table A1.** Comparisons of RR measurement technologies, methods used for evaluations, and findings.

Study	RR Measurement Technology	Methodology	Main Findings
[53]	Ultrasound transceiver	An ultrasound transceiver was adapted as part of Internet of Things and cloud to measure respiration rate in a simulated setting.	Tests in a simulated setting demonstrated respiration rate could be measured in a noncontact manner.
[49]	Microwave Doppler radar	Microwave Doppler radar was used to obtain different dynamics of breathing patterns in addition to the respiration rate.	Doppler radar was found to be effective for respiration rate measurement, identifying breathing patterns, and tidal volumes.

Table A1. Cont.

Study	RR Measurement Technology	Methodology	Main Findings
[36]	Thoracic electrical impedance pneumography	A simple wireless impedance pneumography system for sensing respiration is reported. It was evaluated on fifteen volunteers.	The device could measure the respiratory cycle variations.
[33]	Fiber Mach–Zehnder interferometer (optical approach)	A Mach–Zehnder interferometer was incorporated in a textile belt and attached to the abdomen. The setup was evaluated by measuring the respiration rates of six volunteers.	The setup successfully measured respiration rate in the individuals tested.
[69]	Pulse oximetry	Fifteen healthy adults (mean age $21 \pm 1.2$ years) were recruited, and the sensor was attached to the left index or middle finger.	RR could be determined from pulse oximetry.
[24]	ECG-derived	Several methods were proposed to improve accuracy and reduce computational complexity, accuracy, and power consumption for ECG-derived respiration rate estimation.	The proposed method achieved high QRS detection accuracy (99.18%) and low ECG-derived respiration rate estimation mean absolute error (0.73).
[25]	Single-lead ECG-derived respiration (EDR)	Ten methods of computing single-lead ECG-derived RR (EDR) were compared under different operating conditions.	QRS-slopes-based method outperformed other ECG-derived RR measurement methods.
[70]	Photoplethysmography and capnography	30 healthy volunteers (mean age $43 \pm 12$ years) were recruited to monitor respiratory patterns at various respiratory rates.	Photoplethysmography on the sternum provided measurements of respiratory rate comparable to capnography.
[38]	Infrared thermal imaging	Forty-one adults and 20 children were recruited, and their facial infrared thermal images were recorded. Image processing methods were used to determine respiration rate from the recorded images.	The correlation between respiratory rate measured using infrared thermal imaging and a contact method used for comparison was 0.94.
[40]	Vision (RGB camera)	A phantom study was carried out in a laboratory environment simulating sleep monitoring.	The findings from the study can improve the understanding and applications of camera-based respiration measurement.
[39]	Vision-based	RGB cameras and convolutional neural network were used to automatically detect the region of interest and measure RR.	The method was reported to measure RR with an error of approximately 0.1 bpm.
[54]	Mobile phone and ultrasound	The built-in speaker of a mobile phone was used to generate an ultrasound signal, and the phone's microphone was used to receive the signal reflected from the subject.	The method tracked chest movement and estimated RR under different test conditions.
[71]	Mobile phone application	30 healthy adult subjects were recruited. RR was estimated by determining the median time between breaths obtained by tapping on a mobile phone's screen.	The method resulted in improved efficiency compared to manual counting.

Table A1. Cont.

Study	RR Measurement Technology	Methodology	Main Findings
[31]	Accelerometry	An accelerometer worn on the chest was used to measure RR.	The method estimated RR with a mean difference of 1.9 bpm compared to respiratory inductance plethysmography.
[72]	Review	A review of RR estimation from the electrocardiogram and pulse oximetry (photoplethysmogram, PPG)	Numerous algorithms have been proposed to estimate RR from the electrocardiogram (ECG) and pulse oximetry that provide an opportunity for automated RR measurement.
[8]	Review	Contact and noncontact respiration measurement methods were compared, focusing on children.	Noncontact respiration rate measurement methods are preferable in children due to their higher tolerance, but more developments are needed.
[73]	Systematic review of RR measurement technologies	PubMed, Embase, and Compendex databases were searched for publications through September 2017 to assess RR measurement technologies.	The focus of the paper was RR measurement to identify childhood pneumonia. There is an urgent need for affordable and effective RR measurement technologies.
[7]	Non-experimental survey	A double-blind survey of nurses in Asia Pacific, Middle East, and Western Europe to understand RR measurement practices by nurses.	The study highlighted the need to enhance international nursing education regarding the importance of measuring respiration rate.
[6]	Systematic literature review	Reviewed CINAHL, PubMed, Medline, and Scopus to explore how registered nurses are measuring respiratory rate in adult acute care health settings.	Despite its importance, the review indicated that RR is not being assessed correctly by nursing staff in the acute care environment.
[19]	Review	A discussion of developments in wearable respiratory sensors.	There is a growing interest in wearable respiratory sensors and opportunities for innovations.

## References

1. Webster, L.R.; Karan, S. The physiology and maintenances of respiration: A narrative review. *Pain Ther.* **2020**, *9*, 467–486. [\[CrossRef\]](#) [\[PubMed\]](#)
2. Hill, B.; Annesley, S.H. Monitoring respiratory rate in adults. *Br. J. Nurs.* **2020**, *29*, 12–16. [\[CrossRef\]](#) [\[PubMed\]](#)
3. Fleming, S.; Thompson, M.; Stevens, R.; Heneghan, C.; Plüddemann, A.; Maconochie, I.; Tarassenko, L.; Mant, D. Normal ranges of heart rate and respiratory rate in children from birth to 18 years: A systematic review of observational studies. *Lancet* **2011**, *377*, 1011–1018. [\[CrossRef\]](#) [\[PubMed\]](#)
4. Kelly, C. Respiratory rate 1: Why measurement and recording are crucial. *Nurs. Times* **2018**, *114*, 23–24.
5. Cretikos, M.A.; Bellomo, R.; Hillman, K.; Chen, J.; Finfer, S.; Flabouris, A. Respiratory rate: The neglected vital sign. *Med. J. Aust.* **2008**, *188*, 657–659. [\[CrossRef\]](#)
6. Palmer, J.H.; James, S.; Wadsworth, D.; Gordon, C.J.; Craft, J. How registered nurses are measuring respiratory rates in adult acute care health settings: An integrative review. *Wiley J. Clin. Nurs.* **2023**, *32*, 4515–4527. [\[CrossRef\]](#)
7. Kayser, S.A.; Williamson, R.; Siefert, G.; Roberts, D.; Murray, A. Respiratory rate monitoring and early detection of deterioration practices. *Br. J. Nurs.* **2023**, *32*, 620–627. [\[CrossRef\]](#)
8. Daw, W.; Kingshott, R.; Saatchi, R.; Burke, D.; Holloway, A.; Travis, J.; Evans, R.; Jones, A.; Hughes, B.; Elphick, H. Medical devices for measuring respiratory rate in children: A review. *J. Adv. Biomed. Eng. Technol.* **2016**, *3*, 21–27. [\[CrossRef\]](#)

9. Daw, W.; Kingshott, R.; Saatchi, R.; Elphick, H. Contactless portable respiratory rate monitor (CPRM) accurately measures respiratory rate in sleeping children. *Arch. Dis. Child.* **2016**, *101*, A290–A291. Available online: [https://adc.bmj.com/content/archdischild/101/Suppl\\_1/A290.2.full.pdf](https://adc.bmj.com/content/archdischild/101/Suppl_1/A290.2.full.pdf) (accessed on 30 July 2024). [\[CrossRef\]](#)
10. Daw, W.J.; Kingshott, R.N.; Elphick, H.E. Poor inter-observer agreement in the measurement of respiratory rate in children: A prospective observational study. *BMJ Paediatr. Open* **2017**, *1*, e000173. [\[CrossRef\]](#) [\[PubMed\]](#) [\[PubMed Central\]](#)
11. Daw, W.; Kaur, R.; Delaney, M.; Elphick, H. Respiratory rate is an early predictor of clinical deterioration in children. *Pediatr. Pulmonol.* **2020**, *55*, 2041–2049. [\[CrossRef\]](#)
12. Nakitende, I.; Namujwiga, T.; Dunsmuir, D.; Ansermino, J.M.; Wasingya-Kasereka, L.; Kellett, J. Respiratory rates observed over 15 seconds compared with rates measured using the RRate app. Practice-based evidence from an observational study of acutely ill adult medical patients during their hospital admission. *Acute Med.* **2020**, *19*, 15–20. [\[CrossRef\]](#)
13. Schellander, M.; Schweighofer, B.; Neumayer, M.; Wegleiter, H. Investigation of thermal anemometry with thermistor sensing elements for gas flow measurements in harsh environments. *IEEE Sens. Lett.* **2023**, *7*, 6005304. [\[CrossRef\]](#)
14. Martin, D.P.; Grant, J.J.; Ringwood, J.V. Evaluation of a prototype thermal anemometer for use in low air speed drying measure calculations. *Flow Meas. Instrum.* **2002**, *12*, 385–396. [\[CrossRef\]](#)
15. SOMNOmedics, SOMNOtouch™ RESP. Available online: [https://somnomedics.de/en/solutions/sleep\\_diagnostics/polygraphy-devices/somnotouch-resp/](https://somnomedics.de/en/solutions/sleep_diagnostics/polygraphy-devices/somnotouch-resp/) (accessed on 12 September 2024).
16. AL-Khalidi, F.Q.; Saatchi, R.; Burke, D.; Elphick, H.; Tan, S. Respiration rate monitoring methods: A review. *Pediatr. Pulmonol.* **2011**, *46*, 523–529. [\[CrossRef\]](#)
17. Vitazkova, D.; Foltan, E.; Kosnacova, H.; Micjan, M.; Donoval, M.; Kuzma, A.; Kopani, M.; Vavrinsky, E. Advances in respiratory monitoring: A comprehensive review of wearable and remote technologies. *Biosensors* **2024**, *14*, 90. [\[CrossRef\]](#)
18. Massaroni, C.; Nicolò, A.; Presti, D.L.; Sacchetti, M.; Silvestri, S.; Schena, E. Contact-based methods for measuring respiratory rate. *Sensors* **2019**, *19*, 908. [\[CrossRef\]](#) [\[PubMed\]](#)
19. Yin, Z.; Yang, Y.; Hu, C.; Li, J.; Qin, B.; Yang, X. Wearable respiratory sensors for health monitoring. *Asia Mater.* **2024**, *16*, 8. [\[CrossRef\]](#)
20. Kim, D.; Lee, J.; Park, M.K.; Ko, S.H. Recent developments in wearable breath sensors for healthcare monitoring. *Commun. Mater.* **2024**, *5*, 41. [\[CrossRef\]](#)
21. Van der Linden, M.; Veldhoen, E.S.; Arasteh, E.; Long, X.; Alderliesten, T.; de Goederen, R.; Dudink, J. Noncontact respiration monitoring techniques in young children: A scoping review. *Pediatr. Pulmonol.* **2024**, *59*, 1871–1884. [\[CrossRef\]](#)
22. Chan, E.D.; Chan, M.M.; Chan, M.M. Pulse oximetry: Understanding its basic principles facilitates appreciation of its limitations. *Respir. Med.* **2013**, *107*, 789–799. [\[CrossRef\]](#)
23. Elliott, M.; Baird, J. Pulse oximetry and the enduring neglect of respiratory rate assessment: A commentary on patient surveillance. *Br. J. Nurs.* **2019**, *28*, 1256–1259. [\[CrossRef\]](#)
24. Fan, J.; Yang, S.; Liu, J.; Zhu, Z.; Xiao, J.; Chang, L.; Lin, S.; Zhou, J. A high accuracy & ultra-low power ECG-derived respiration estimation processor for wearable respiration monitoring Sensor. *Biosensors* **2022**, *12*, 665. [\[CrossRef\]](#)
25. Varon, C.; Morales, J.; Lázaro, J.; Orini, M.; Deviaene, M.; Kontaxis, S.; Testelmans, D.; Buyse, B.; Borzée, P.; Sörnmo, L.; et al. A comparative study of ECG derived respiration in ambulatory monitoring using the single-lead ECG. *Sci. Rep.* **2020**, *10*, 5704. [\[CrossRef\]](#)
26. Bawua, L.K.; Miaskowski, C.; Hu, X.; Rodway, G.W.; Pelter, M.M. A Review of the Literature on the Accuracy, Strengths, and Limitations of Visual, Thoracic Impedance, and Electrocardiographic Methods Used to Measure Respiratory Rate in Hospitalized Patients. *Ann. Noninvasive Electrol. Cardiol.* **2021**, *26*, e12885. [\[CrossRef\]](#)
27. Saatchi, R.; Elphick, H.; Rowson, J.; Wesseler, M.; Marris, J.; Shortland, S.; Thomas, L. Development of a new prototype paediatric central sleep apnoea monitor. *Technologies* **2024**, *12*, 116. [\[CrossRef\]](#)
28. Jarchi, D.; Rodgers, S.J.; Tarassenko, L.; Clifton, D.A. Accelerometry-based estimation of respiratory rate for post-intensive care patient monitoring. *IEEE Sens. J.* **2018**, *18*, 4981–4989. [\[CrossRef\]](#)
29. Siqueira, A.; Spirandeli, A.F.; Moraes, R.; Zarzoso, V. Respiratory waveform estimation from multiple accelerometers: An optimal sensor number and placement analysis. *IEEE J. Biomed. Health Inform.* **2019**, *23*, 1507–1515. [\[CrossRef\]](#)
30. De Fazio, R.; Stabile, M.; De Vittorio, M.; Velázquez, R.; Visconti, P. An Overview of wearable piezoresistive and inertial sensors for respiration rate monitoring. *Electronics* **2021**, *10*, 2178. [\[CrossRef\]](#)
31. Ryser, F.; Hanassab, S.; Lamercy, O.; Werth, E.; Gassert, R. Respiratory analysis during sleep using a chest-worn accelerometer: A machine learning approach. *Biomed. Signal Process. Control* **2022**, *78*, 104014. [\[CrossRef\]](#)
32. Schipper, F.; van Sloun, R.J.G.; Grassi, A.; Derkx, R.; Overeem, S.; Fonseca, P. Estimation of respiratory rate and effort from a chest-worn accelerometer using constrained and recursive principal component analysis. *IOP Publ. Physiol. Meas.* **2021**, *42*, 1–16. [\[CrossRef\]](#) [\[PubMed\]](#)
33. Cao, Z.; Shao, M.; Yuan, Y.; Ma, X.; Yu, Y.; Qiao, X. In-fiber Mach-Zehnder interferometer for wearable respiration measurement. *Sens. Actuators A Phys.* **2023**, *364*, 114806. [\[CrossRef\]](#)



34. Carry, P.Y.; Baconnier, P.; Eberhard, A.; Cotte, P.; Benchetrit, G. Evaluation of respiratory inductive plethysmography: Accuracy for analysis of respiratory waveforms. *Chest* **1997**, *111*, 910–915. [CrossRef] [PubMed]
35. Hernández, L.; Ballester, E.; Farré, R.; Badia, J.R.; Lobelo, R.; Navajas, D.; Montserrat, J.M. Performance of nasal prongs in sleep studies. *Chest* **2001**, *119*, 442–450. [CrossRef] [PubMed]
36. Aqueveque, P.; Gómez, B.; Monsalve, E.; Germany, E.; Ortega-Bastidas, P.; Dubo, S.; Pino, S.J. Simple wireless impedance pneumography system for unobtrusive sensing of respiration. *Sensor* **2020**, *20*, 5228. [CrossRef]
37. Alkali, A.H.; Saatchi, R.; Elphick, H.; Burke, D. Thermal image processing for real-time non-contact respiration rate monitoring. *IET Circuits Devices Syst.* **2017**, *11*, 142–148. [CrossRef]
38. Elphick, H.; Alkali, A.; Kingshott, R.; Burke, D.; Saatchi, R. Exploratory study to evaluate respiratory rate using a thermal imaging camera. *Respiration* **2019**, *97*, 205–212. [CrossRef]
39. Hwang, H.; Lee, K.; Lee, E.C. A real-time remote respiration measurement method with improved robustness based on a CNN model. *Appl. Sci.* **2022**, *12*, 11603. [CrossRef]
40. Wang, W.; den Brinker, A.C. Algorithmic insights of camera-based respiratory motion extraction. *Physiol. Meas.* **2022**, *43*, 1–20. [CrossRef]
41. Addison, P.S.; Antunes, A.; Montgomery, D.; Smit, P.; Borg, U.R. Robust non-contact monitoring of respiratory rate using a depth camera. *J. Clin. Monit. Comput.* **2023**, *37*, 1003–1010. [CrossRef]
42. Umeda, A.; Ishizaka, M.; Ikeda, A.; Miyagawa, K.; Mochida, A.; Takeda, H.; Takeda, K.; Fukushi, I.; Okada, Y.; Gozal, D. Recent insights into the measurement of carbon dioxide concentrations for clinical practice in respiratory medicine. *Sensors* **2021**, *21*, 5636. [CrossRef] [PubMed]
43. Sankaran, D.; Zeinali, L.; Iqbal, S.; Chandrasekharan, P.; Lakshminrusimha, S. Non-invasive carbon dioxide monitoring in neonates: Methods, benefits, and pitfalls. *J. Perinatol.* **2021**, *41*, 2580–2589. [CrossRef] [PubMed]
44. Kano, S.; Jarulertwathana, N.; Mohd-Noor, S.; Hyun, J.K.; Asahara, R.; Mekaru, H. Respiratory monitoring by ultrafast humidity sensors with nanomaterials: A review. *Sensors* **2022**, *22*, 1251. [CrossRef] [PubMed]
45. Doheny, E.P.; O’Callaghan, B.P.F.; Fahed, V.S.; Liegey, J.; Goulding, C.; Ryan, S.; Lowery, M.M. Estimation of respiratory rate and exhale duration using audio signals recorded by smartphone microphones. *Biomed. Signal Process. Control* **2023**, *80*, 104318. [CrossRef]
46. Nam, Y.; Reyes, B.A.; Chon, K.H. Estimation of Respiratory Rates Using the Built-in Microphone of a Smartphone or headset. *IEEE J. Biomed. Health Inform.* **2016**, *20*, 1493–1501. [CrossRef]
47. Yabuki, S.; Toyama, H.; Takei, Y.; Wagatsuma, T.; Yabuki, H.; Yamauchi, M. Influences of environmental noise level and respiration rate on the accuracy of acoustic respiration rate monitoring. *J. Clin. Monit. Comput.* **2018**, *32*, 127–132. [CrossRef] [PubMed]
48. Edanami, K.; Sun, G. Medical radar signal dataset for non-contact respiration and heart rate measurement. *Data Brief* **2022**, *40*, 107724. [CrossRef]
49. Lee, Y.S.; Pathirana, P.N.; Steinfort, C.L.; Caelli, T. Monitoring and analysis of respiratory patterns using microwave doppler radar. *Med. Imaging Diagn. Radiol.* **2014**, *2*, 1800912. [CrossRef]
50. Yang, F.; He, Z.; Fu, Y.; Li, L.; Jiang, K.; Xie, F. Noncontact detection of respiration rate based on forward scatter radar. *Sensors* **2019**, *19*, 4778. [CrossRef]
51. van Loon, K.; Breteler, M.J.M.; van Wolfwinkel, L.; Leyssius, A.T.R.; Kossen, S.; Kalkman, C.J.; van Zaane, B.; Peelen, L.M. Wireless non-invasive continuous respiratory monitoring with FMCW radar: A clinical validation study. *J. Clin. Monit. Comput.* **2016**, *30*, 797–805. [CrossRef]
52. Yoo, S.K.; Lee, J. Radar-based detection of respiration rate with adaptive harmonic quefrency selection. *Sensors* **2020**, *20*, 1607. [CrossRef] [PubMed]
53. Abdulqader, T.; Saatchi, R.; Elphick, H. Respiration measurement in a simulated setting incorporating the internet of things. *Technologies* **2021**, *9*, 30. [CrossRef]
54. Ge, L.; Zhang, J.; Wei, J. Single-frequency ultrasound-based respiration rate estimation with smartphones. *Comput. Math. Methods Med.* **2018**, *2018*, 3675974. [CrossRef]
55. Arlotto, P.; Grimaldi, M.; Naeck, R.; Ginoux, J.-M. An ultrasonic contactless sensor for breathing monitoring. *Sensors* **2014**, *14*, 15371–15386. [CrossRef] [PubMed]
56. Daw, W. Measuring Respiratory Rate in Children. Ph.D. Dissertation, The University of Sheffield, Sheffield, UK, 2018. Available online: <https://etheses.whiterose.ac.uk/id/eprint/21389/> (accessed on 16 May 2025).
57. Steinhart, J.S.; Hart, S.R. Calibration curve for thermometers. *Deep. Sea Res. Oceanogr. Abstr.* **1968**, *15*, 497–503. [CrossRef]
58. Will, J.P.; Krut, N.P.; Venner, C.H. An experimental study of forced convective heat transfer from smooth, solid spheres. *Int. J. Heat Mass Transf.* **2017**, *109*, 1059–1067. [CrossRef]
59. Analogue Devices. OP200 Data Sheet, Dual Low Offset, Low Power, Operational Amplifier. Available online: <https://www.analog.com/media/en/technical-documentation/data-sheets/op200.pdf> (accessed on 15 August 2024).



60. STMicroelectronics. Available online: <https://www.st.com/en/microcontrollers-microprocessors/stm32f407-417/products.html> (accessed on 4 April 2025).
61. STM32F4DIS-LC. Available online: <https://www.farnell.com/datasheets/1671831.pdf> (accessed on 4 April 2025).
62. Vishay. Optocoupler. Available online: <https://www.vishay.com/docs/83725/4n25.pdf> (accessed on 7 April 2025).
63. Vishay. IRF530 Power MOSFET. Available online: <https://www.vishay.com/docs/91019/irf530.pdf> (accessed on 7 April 2025).
64. Yucel Lead Acid Rechargeable Battery, 12 V, 0.8 h, C20. Available online: <https://www.yuasa.co.uk/> (accessed on 16 August 2024).
65. Ansmann. Battery Charger for Lead Acid 12 V 900 mA, Manufacturer Part Number 9564006-1. Available online: <https://www.ansmann.de/en> (accessed on 16 August 2024).
66. 7805T Datasheet. Available online: <https://www.alldatasheet.com/view.jsp?Searchword=7805T&sField=1> (accessed on 7 April 2025).
67. LD1117V33 STMicroelectronics. Available online: [https://www.digikey.co.uk/en/products/detail/stmicroelectronics/LD1117V33/586012?srltid=AfmBOooNdTX0upFJWFTn7CXDWi4E-lbXgrJYI-Sn6IpWBjYTrp\\_z16ND](https://www.digikey.co.uk/en/products/detail/stmicroelectronics/LD1117V33/586012?srltid=AfmBOooNdTX0upFJWFTn7CXDWi4E-lbXgrJYI-Sn6IpWBjYTrp_z16ND) (accessed on 7 April 2025).
68. MHRA. The Medicines and Healthcare Products Regulatory Agency. Available online: <https://www.gov.uk/government/news/welcome-to-our-new-mhra-website> (accessed on 7 April 2025).
69. Chon, K.H.; Dash, S.; Ju, K. Estimation of Respiratory Rate from Photoplethysmogram Data Using Time–Frequency Spectral Estimation. *IEEE Trans. Biomed. Eng.* **2009**, *56*, 2054–2063. [\[CrossRef\]](#)
70. Henricson, J.; Glasin, J.; Rindebratt, S.; Wilhelms, D. Respiratory rate monitoring in healthy volunteers by central photoplethysmography compared to capnography. *J. Biophotonics* **2022**, *15*, e202100270. [\[CrossRef\]](#)
71. Karlen, W.; Gan, H.; Chiu, M.; Michelle, C.; Dunsmuir, D.; Zhou, C.; Dumont, G.A.; Ansermino, M. Improving the accuracy and efficiency of respiratory rate measurements in children using mobile devices. *PLoS ONE* **2014**, *9*, e99266. [\[CrossRef\]](#)
72. Charlton, P.H.; Birrenkott, D.A.; Bonnici, T.; Pimentel, M.A.F.; Johnson, A.E.W.; Alastruey, J.; Tarassenko, L.; Watkinson, P.J.; Beale, R.; Clifton, D.A. Breathing rate estimation from the electrocardiogram and photoplethysmogram: A review. *IEEE Rev. Biomed. Eng.* **2018**, *11*, 2–20. [\[CrossRef\]](#)
73. Ginsburg, A.S.; Lenahan, J.L.; Izadnegahdar, R.; Ansermino, J.M. A systematic review of tools to measure respiratory rate in order to identify childhood pneumonia. *Am. J. Respir. Crit. Care Med.* **2018**, *197*, 1116–1127. [\[CrossRef\]](#) [\[PubMed\]](#)

**Disclaimer/Publisher’s Note:** The statements, opinions and data contained in all publications are solely those of the individual author(s) and contributor(s) and not of MDPI and/or the editor(s). MDPI and/or the editor(s) disclaim responsibility for any injury to people or property resulting from any ideas, methods, instructions or products referred to in the content.